Study of the Galactic Photon Dominated Region(PDR) in ρ Ophiuchus A

A Thesis

submitted to

Indian Institute of Science Education and Research, Pune
in partial fulfillment of the requirements for the
BS-MS Dual Degree Programme

by

Spandan Choudhury

Indian Institute of Science Education and Research, Pune
Dr. Homi Bhabha Road,
Pashan, Pune 411008, INDIA.

April, 2018

Supervisor: **Dr. Bhaswati Mookerjea**
© **Spandan Choudhury** 2018

i

Certificate

This is to certify that this thesis entitled **Study of the Galactic Photon Dominated Region(PDR) in ρ Ophiuchus A** submitted towards the partial fulfilment of the BS-MS dual degree programme at the Indian Institute of Science Education and Research, Pune represents original research carried out by **Spandan Choudhury** at **Tata Institute of Fundamental Research, Mumbai**, under the supervision of **Dr. Bhaswati Mookerjea** during the academic year 2017-2018.

20/3/2018

Student
Spandan Choudhury

Supervisor
Dr. Bhaswati Mookerjea

This thesis is dedicated to my parents.

Declaration

I hereby declare that the matter embodied in the report entitled "Study of the Galactic Photon Dominated Region(PDR) in ρ Ophiuchus A" are the results of the investigations carried out by me at the Department of Astronomy and Astrophysics, Tata Institute of Fundamental Research, Mumbai under the supervision of Dr. Bhaswati Mookerjea and the same has not been submitted elsewhere for any other degree.

Student
SPANDAN CHOUDHURY

Supervisor
DR. BHASWATI MOOKERJEA

Acknowledgments

I would like to take this opportunity to thank my supervisor, Dr. Bhaswati Mookerjea, for her guidance and continued support throughout this project. It has been an immense learning experience, and a great journey.

I would also like to thank Dr. Franck Le Petit and Dr. Jacques Le Bourlot, for their help in navigating through aspects of the Meudon PDR Code. Their ready responses and helpful suggestions were much appreciated.

I would like to thank my parents, family and friends, for their reliable support whenever I needed it.

Finally, I would like to thank IISER, Pune, for allowing its students to pursue the MS project at an institute of their choice. This was a great opportunity, and I am really grateful to have been able to explore a new institute and an interesting field of study.

x

Abstract

Photon Dominated Regions(PDR) are predominantly neutral regions in the interstellar medium(ISM), which contains both atomic and molecular gas. Physical properties of the PDRs are governed primarily by far-ultraviolet photons from nearby stars, or the interstellar radiation field. PDRs provide a unique opportunity to study the effect of young massive stars on the interstellar gas.

In this project, we study the PDR near the active star forming region ρ Oph A. We have used new, velocity resolved [CII] observations, obtained with the Stratospheric Observatory For Infrared Astronomy (SOFIA), as the primary dataset. We also use observations in known PDR tracers, neutral oxygen(from Herschel Space Observatory archive) and PAH molecules(from Spitzer Space Telescope archive); as well as CO, from the archival data of James Clerk Maxwell Telescope(JCMT). Using these tracers, we study the structure and distribution of gas in the PDR.

We have used a numerical model for PDRs, the Meudon PDR code (Le Petit et al., 2006 [29]) to interpret the observed intensities of spectral lines to constrain the physical conditions (hydrogen number density ($n(H)$) and far-ultraviolet radiation strength) in ρ Oph A. We have also extensively used the PDR model to study, in general, the variation of intensities of major PDR tracers as a function of density, intensity of FUV radiation field and metalicity.

Contents

List of Figures

List of Tables

Chapter 1

Introduction

The process of star formation takes place in the interstellar medium(ISM) in galaxies. The stars, in turn, inject elements into the ISM during their evolution. Also, properties of the ISM are regulated, to a large extent, by the radiation from massive stars. This, in a way, acts as a feedback mechanism, in the sense that the newly-formed stars directly influence the structure and chemistry of regions of active star formation. The ultraviolet radiation from massive stars ionise the gas in the close neighbourhood of the star. Beyond this ionised region, the photons do not have enough energy to ionise hydrogen (ionisation energy 13.6 eV), but can still ionise elements like carbon, which have lower ionisation energy (11.26 eV). This creates a predominantly neutral region after the H^+ layer, where we find species such as H, H_2, O^0, C^+, C^0 and CO. The heating and the chemistry in such regions are strongly influenced by incident far-ultraviolet(FUV) photons with energy 6 eV $< h\nu <$ 13.6 eV. These regions are known as Photon Dominated Regions, or PDRs.

PDRs are the source of most of the non-stellar infrared(IR) emission, as well as millimeter and sub-millimeter emission of CO. All of the atomic gas, and most ($\sim 90\%$) of the molecular gas is found inside PDRs. Due to the clumpy structure of the PDRs, they are more than just surface phenomenon. These regions provide direct insight into the chemical evolution of the ISM, influenced by FUV photons. PDRs are also the perfect laboratory to study the radiation-induced feedback mechanisms that may affect the column densities of gas in giant molecular clouds, thus regulating the rate of star formation.(B. Mookerjea et al., 2006 [37]) Observation of nearby PDRs provide better spatial resolution, which helps in understanding the structure of the region. In this project, we study the molecular cloud L1688 in the con-

stellation Ophiuchus, a dark cloud located at a distance ~ 130 pc. We try to understand the physical properties of the PDR located in ρ Oph, near the B4-type star S1 (hence, the PDR is referred to hereafter as the S1 PDR, or ρ Oph PDR). The dense core ρ Oph A, which is an active site of star formation, is located just south-west to this PDR. The core contains several pre-stellar and protostellar objects at different stages of their evolution. So, it is a region of great interest, and has been studied in detail. Since ρ Oph A is in close proximity to the S1 PDR, it is likely that the PDR influences the process of star formation taking place there. If so, then the PDR in question needs to be studied in detail, in regards to the star formation in ρ Oph A core. However, there has not been many detailed studies about the PDR in the existing literature.

Here, we use the recent [CII] 158 μm ($^2P_{3/2}$ - $^2P_{1/2}$ transition of C^+) data obtained from SOFIA observations to study the S1 PDR. We compare our observations with maps of the region in other tracers such as CO and its isotopomers (^{13}CO and $C^{18}O$), neutral oxygen and dust continuum (at 8 μm and 70 μm) to study the temperature and density distribution of gas and dust in the PDR. The [OI] transitions considered are the fine-structure transitions $^3P_1$ - $^3P_2$ (63 μm) and $^3P_0$ - $^3P_1$ (145 μm). For CO and its isotopomers, we use the rotational transition of J=3-2. Since carbon has a relatively low ionisation energy of 11.26 eV, C^+ emission can originate both in the ionised (H^+) region, and the neutral (atomic and molecular) cloud. Using the velocity information in our data, we can separate the different contributions and understand the distribution of C^+ in the region. In Chapter 3, we present the results from these observations, followed by discussions on them in Chapter 4.

In the second part of the project, we use a numerical model for PDRs, to study the effects of different conditions and parameters on the PDR properties. We consider parameters such as the density of the cloud, strength of radiation incident on it and the metallicity of the region; and how they affect the distribution of gas in the PDR. The models used, and the parameter space considered, are discussed in Chapter 5. In the following chapter, Chapter 6, we discuss the results obtained from the PDR models. We also compute line intensity ratios from our observations of the S1 PDR, and and by comparison with the model predicted trends, try to determine the density and radiation field strength in the observed region.

Chapter 2

Photon Dominated Region (PDR)

As mentioned, Photon Dominated Regions, or PDRs, are predominantly neutral regions of gas and dust in the interstellar medium(ISM), whose properties are governed by far-ultraviolet (FUV) photons. These photons dominate the heating and the chemical processes in PDRs. The study of PDRs is essentially a study of the effects of FUV radiation on the structure, chemistry, and evolution of the neutral ISM. PDRs can be divided broadly into two categories based on their density and FUV illumination : (i) low-excitation diffuse clouds, and (ii) dense, highly illuminated clouds.

PDRs are modelled as parallel slab cloud structures, of gas and dust. They are illuminated from one, or both ends by FUV flux from nearby massive stars, or the interstellar radiation field(ISRF). A PDR is characterised by a number of physical parameters such as number density of atomic hydrogen (n_H), temperature of the cloud (T_k), FUV radiation strength (χ) and the optical thickness (A_V). The incident FUV flux, relative to the average interstellar flux in the energy range 6-13.6 eV, is denoted by G_0 .

The heating in PDRs is regulated by the incoming FUV photons. Photo-electric effect on the dust grains dominate the heating process. The photons have enough energy to eject electrons from the dust particles, and these photo-electrons carry their kinetic energy to the gas. Another contribution to the heating comes from the formation of H_2 on the grain surface. The formation reaction is exothermic, and releases heat to the surrounding. Photo-dissociation of molecules and photo-ionisation of atoms also contribute to the heating. Apart from these, ionisation by cosmic rays plays a part in PDR heating, too. The cooling process is regulated mainly by discrete transitions following collisional excitation. The dominant

lines are [CII] 158 μm and [OI] 63 μm and 145 μm. Deeper into the cloud, the rotational transitions of CO dominate the cooling, as most of the gas is molecular.
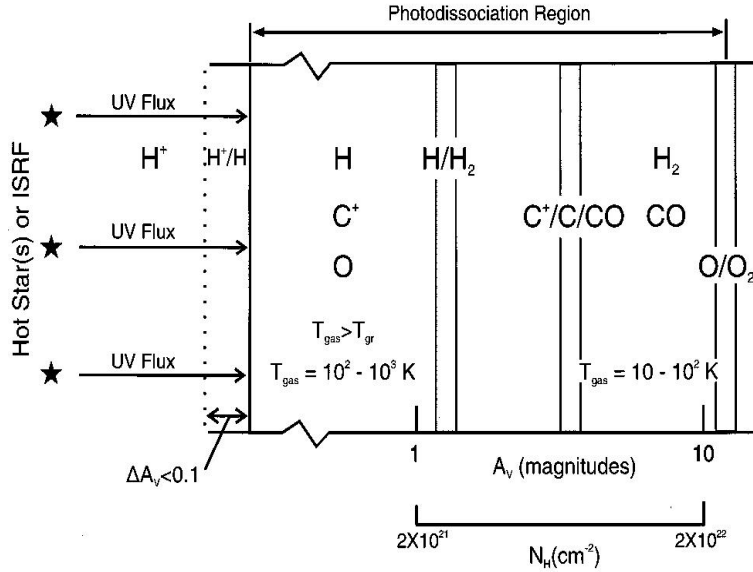
Figure 2.1: Stratification of a PDR, illuminated from the left. The figure shows distribution of different species, that are mostly found in PDRs. (figure from Hollenbach & Tielens, 1999 [21])

The distribution of gas in a PDR is highly influenced by the FUV flux incident on it. Figure 2.1 roughly shows the overall general structure of a PDR, illuminated from one side. Just outside the PDR boundary, towards the illuminating source, lies the HII region. The FUV photons are not energetic enough to ionise hydrogen, but can still dissociate most molecules. The temperature of the PDR is maximum near the edge towards the FUV source, and decreases deeper into the cloud. At the edge, hydrogen and oxygen are in atomic form (both have ionisation energy $\approx$13.6 eV), and carbon is singly ionised (ionisation energy $\sim$ 11.26 eV). The H_2 present here is vibrationally excited. The temperature in this region exceeds 100 K. The HI region extends to optical depth, $A_V \sim 2$, upto the HI/H_2 interface. The C$^+$ layer is stretched til the C$^+$/CI/CO interface at $A_V \sim 4$, and the region of atomic oxygen extends to $A_V \sim 5 - 10$. These different slabs are classified after the dominating form of an element. At the different interfaces, the dominant variant changes from ionised/atomic to atomic/molecular. The region at $A_V \sim 3 - 5$ is partially dissociated, as species such as H_2, O, C and CO are present. The temperature there is $\sim$ 100K. An O^0/O_2 interface at $A_V \sim 10$, where O_2 is not appreciably photo-dissociated, marks the extent of the PDR. In PDRs, H_2 formation is catalysed by adsorption of atomic hydrogen onto dust surface,

4

and its destruction is primarily due to photo-dissociation by the FUV radiation field. For amount of H_2 to remain constant in the line of sight (LoS), the number density of HI (n_H) must increase faster than the radiation field. For species formed by two-body interaction, and whose destruction is mediated by photo-dissociation, the column densities depend on the ratio n_H/χ (number density of atomic hydrogen, to the FUV radiation strength).

Dense PDRs are high-density, neutral, atomic or molecular clouds, in young stellar environment. They are characterised by FUV illumination from one side, and high optical extinction. At the cloud edge, the main heating mechanism is photo-electric effect on dust. The highest temperature region is not exactly at the edge, but is slightly inside. Assuming that the PDR is viewed face-on, the different line intensities can be computed. The exact intensities are difficult to compare with observed data directly, due to various possible errors, but ratios of line intensities from a region can be used to determine the physical conditions present. The ratio of intensities of H_2 lines 2-1 S(1) and 1-0 S(1) is sometimes used as an indicator of presence of shock in the cloud.

2.1   PDR in ρ Oph A : the S1 PDR

In this project, we focus our study on a galactic PDR, in the region of ρ Ophiuchus A(referred to here as S1 PDR). The S1 PDR is in the shape of a spherical shell at a distance < 0.1 pc from the B4-type star S1. This star is the primary source of FUV photons for the PDR. The other major FUV source is HD147889, a B2.5 star, which is slightly more massive and more luminous, but at a much larger distance of > 0.5 pc in the south-west direction. The surface temperatures of S1 and HD147889 are 16000 K and 20000 K, respectively (Liseau et al, 2015 [31]). A composite map of the region in different tracers, is shown in Figure 2.2. The main FUV illuminating source, S1, is shown, along with the molecular core next to the PDR, and a known protostar molecular outflow in the proximity.

The LSR velocity for the region is 2-4 km/s. The emission in CO is spread over velocity range -3 km/s to 8 km/s, and a self-absorption feature is seen for 2.0-5.5 km/s. ^{13}CO and $C^{18}O$, which trace a denser column density, are seen at 0-7 km/s and 2-4 km/s, respectively (White et al, 2015 [56]). Emission at higher offsets from v_{lsr} is primarily originated at the molecular outflow from the class 0 source VLA1623. The red-shifted wing of the molecular
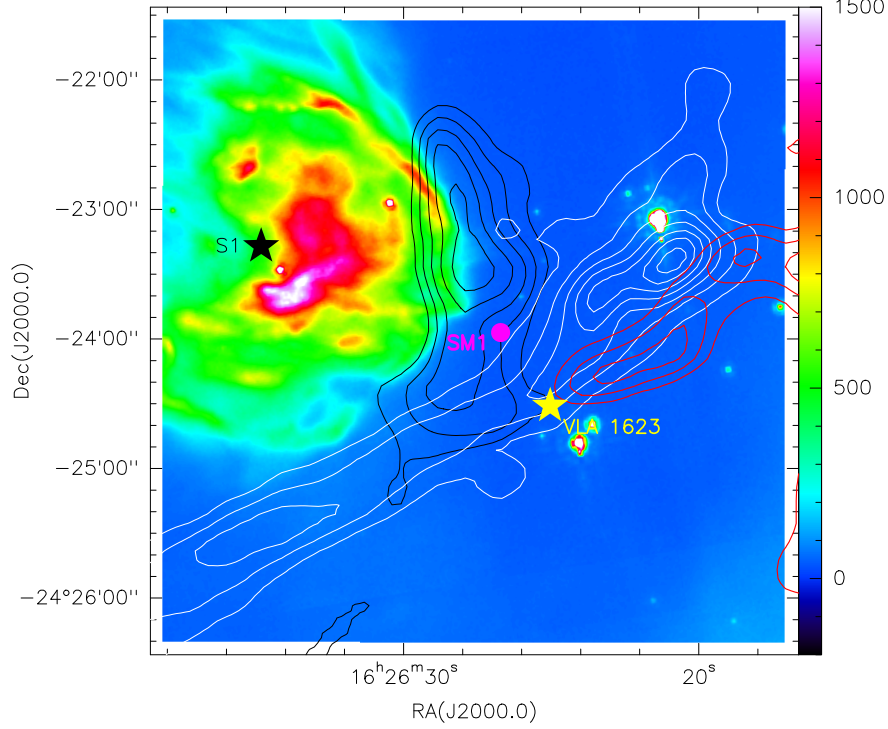
Figure 2.2: Map of the region, showing S1 PDR. The colour map is of 8 μm continuum emission, and the black contours show $C^{18}O$ J=3-2. The white and red contours are of CO J=3-2, and show the blue- and red-shifted wings of the molecular jet, respectively, associated with the protostar VLA1623. The position star S1 is shown as a black star, and the yellow star shows VLA1623. The dense star-forming core, SM1 is also shown.

outflow is at velocity -6 km/s to +2 km/s , and the blue-shifted wing is at 4-15 km/s (Murillo and Lai, 2013 [38]).

The source S1 is in a low-density bubble of carbon, which is the origin of the [CII] emission. The grains in this region has size $\sim 0.1\mu$m, and the mass of the region is estimated to be 7 x $10^{-4} M_\odot$. Scattering by these grains account for the emission at near and far IR. There are two YSOs(Young Stellar Objects) embedded in the region, each of luminosity $\sim 2\ L_\odot$; but they have negligible contribution to the FUV flux. (Liseau et al, 2015 [31])

From H_2 pure rotational transition (Larsson and Liseau, 2017 [27]), it is estimated that the interface towards S1 has temperature of $T \geq 10^3$K. The kinetic temperature is determined from observations of $C^{18}O$, which is assumed to be optically thin. In regions where the line is optically thick, other tracers have to be employed for estimating T_{kin}.

Chapter 3

Observations and Results

3.1 Observations

3.1.1 [CII]

In this project, [CII] 158 μm has been used as the primary tracer to study the S1 PDR. The corresponding observation was made using the instrument GREAT (**G**erman **RE**ceiver for **A**stronomy at **T**erahertz Frequencies) aboard the airborne SOFIA observatory (SOFIA : Stratospheric Observatory for Infrared Astronomy). SOFIA is a 2.7 m telescope, with effective aperture of 2.5 m; and has a pointing accuracy of $\sim 0.5''$. The beam size for the telescope is diffraction limited, and in the case of GREAT, it is $14.1''$ at 158 μm. GREAT is a dual channel heterodyne instrument that provides high resolution spectra in several windows in the frequency range 0.49-4.747 THz. The seven-beam array in its low-frequency-array configuration operates at 158 μm. (Details from SOFIA Science Centre data, https://www.sofia.usra.edu/science/instruments/great)

3.1.2 CO, ^{13}CO and C^{18}O

The observations in J=3-2 transition of CO and its isotopologues, ^{13}CO and C^{18}O, were used to map the cold, dense molecular region, just outside the S1 PDR. These observations were

obtained from the online archive for the James Clerk Maxwell Telescope (JCMT), situated near the summit of Mauna Kea in Hawaii. Situated at an altitude of 4092m, JCMT is a single-dish telescope of diameter 15 m. Its pointing accuracy is $\sim 2''$. The data was taken using the receiver HARP (Heterodyne Array Receiver Program), which is a single-sideband(SSB) array receiver with 16 SIS mixers. HARP can be tuned to operate at frequencies in the range 325-375 GHz, and has a instantaneous bandwidth of ~ 2 GHz. The beamwidth of the instrument is $\sim 14''$. (From JCMT homepage, https://www.eaobservatory.org/jcmt/public/jcmt/)

3.1.3   [OI] : 63 μm and 145 μm

The data for neutral oxygen lines at 63 and 145 μm were taken from the archives of the infrared space observatory Herschel. The observations were done using the instrument PACS (Photoconductor Array Camera and Spectrometer). The telescope's primary mirror has diameter of 3.5 m. It has a pointing accuracy of $\sim 3.7''$. PACS is a photometer and mid-resolution spectrometer. It employs four detector arrays (two bolometer arrays and two Ge:Ga photoconductor arrays), and operates in wavelengths in the range 60-210 μm. The spectral resolutions at 63 μm and 145 μm are $\sim$3500 and $\sim$1000, respectively (Larsson & Liseau, 2017 [27]). This corresponds roughly to 100 km/s and 300 km/s in velocity. Thus, for the dataset used, we do not have resolved spectra. (https://herschel.jpl.nasa.gov/ and links therein)

3.1.4   Dust Continuum

To study the distribution of dust in the region, we have employed two continuum maps, at 8 μm and at 70 μm. The 70 μm map was obtained from the archives of the aforementioned instrument PACS, in the Herschel Space Observatory. The 8 μm map was taken from archival data of the Spitzer Space Telescope, which has a diameter of 0.85 m. The instrument used in is IRAC (InfraRed Array Camera). IRAC is a four-channel camera that provides simultaneous $5.2' \times 5.2'$ images at 3.6, 4.5, 5.8, and 8 microns. The instrument observes two fields of view simultaneously with centers about $6.5'$ apart, leaving a gap of about $1.5'$ between the fields. (Spitzer documentation, https://irsa.ipac.caltech.edu/data/SPITZER/docs/irac/highleveloverview/)

3.2 Results

3.2.1 [CII] emission

In this section, we present a map of the integrated [CII] emission in the region(Figure 3.1). The map shows emission of [CII] from 0 km/s to 7 km/s in velocity.

As seen in Figure 3.1, [CII] 158 μm maps a nearly spherical region near the B4-type star S1. In the figure, the positions of the primary FUV source, S1 and the class 0 source, VLA1623, are shown. VLA1623 has a known, highly collimated molecular outflow associated with it(shown in Figure 2.2). The coordinates (J2000) for S1 are RA = 16h26m35.2s, Dec = -24°23′17″ (Gagné, Skinner and Daniel, 2004 [15]), and those for VLA1623 are RA = 16h26m26.39s, Dec = $-24°24′30.9″$ (taken from SIMBAD Astronomical Database : http://simbad.u-strasbg.fr/simbad/).
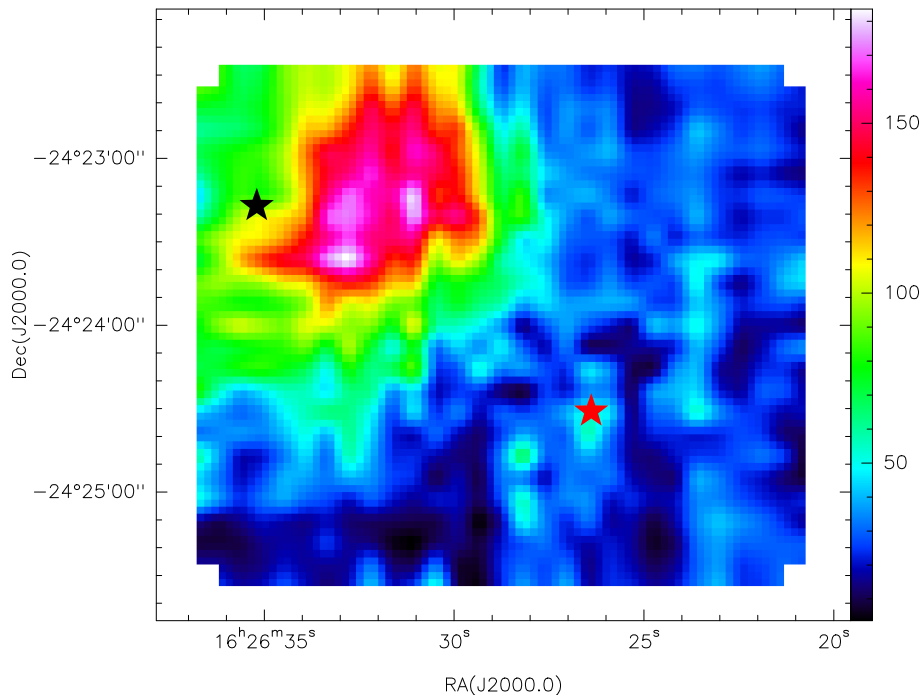

Figure 3.1: [CII] 158 μm observation in the ρ Oph PDR, showing integrated emission between 0 km/s to 7 km/s. The black star is the FUV illumination source S1, and the red star is VLA1623 (a class 0 source).

The [CII] map shows the extent of the hot, low density region. As seen from the map, the region exists in the neighbourhood of S1, and extends upto the molecular cloud to the

west. The distribution of the emission indicates inhomogeneous, clumpy nature of the gas. It is to be noted that most of the [CII] emission is contained in a radius of < 0.1 pc around S1.
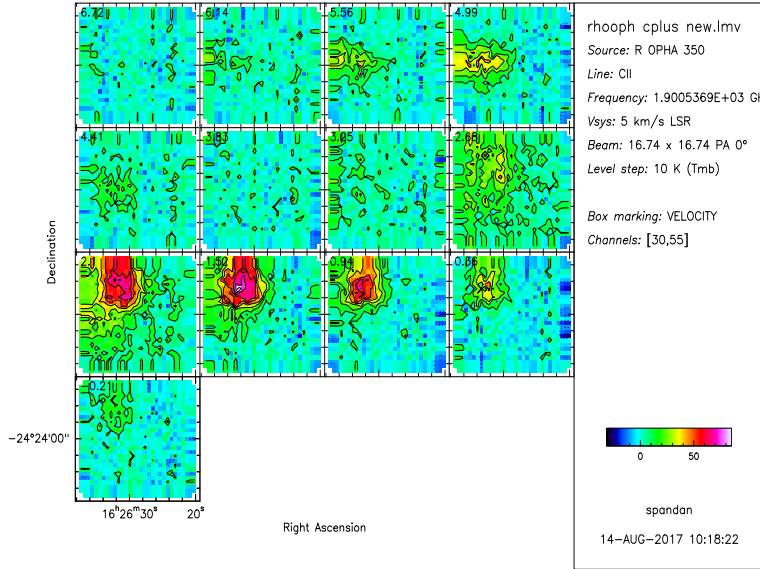

Figure 3.2: Channel map of [CII]. Each panel corresponds to 0.58 km/s. Co-ordinates (RA and Dec) are in J2000. Each panel in the figure shows the integrated emission in a small range around a central velocity, which is indicated at the top left corner of the panel.

Figure 3.2 show the velocity distribution of C^+ emission. In the figure, two apparent components are seen, around v $\sim$ 2 km/s and v $\sim$ 5 km/s. These two components are, however not spatially separated, both show up in the same area near S1. Most of the emission is seen around the velocity of $\sim$ 2 km/s. The two components might arise from two actually different regions in the same line of sight, or, they might appear to be two separate components due to self-absorption by a foreground cold cloud. In the latter case, the emission originates from a single region in the PDR, but is absorbed partly by a colder gas lying in the line of sight. Due to the lower temperature, the Doppler broadening in the foreground cloud is less than that in the emitting cloud. Hence, the absorbed radiation has a narrower profile. Due to this, there will be a drop in the observed intensity for the central velocities, and the spectra will appear to have two components. In order to to conclude on the origin of the components, we need to compare the data with that of other tracers, and look at the detailed individual spectra.

10

3.2.2 CO and its Isotopologues

Here, we present the observational data for CO, and its rarer isotopologues, ^{13}CO and C^{18}O. For all three, we have taken the data for low-J transition(J=3-2) in this project. This line traces the cold, dense molecular cloud, in contrast to the hot, low density region, traced by [CII]. Due to high column density of CO, in some part of the map, the line is optically thick. In that case, for a correct representation of the distribution, we need to switch to rarer isotopes, such as ^{13}CO and C^{18}O. The much rarer C^{18}O is assumed to be optically thin for the entire region of interest. The maps for these tracers are presented in Figure 3.3.

(a) CO

(b) ^{13}CO

(c) C^{18}O
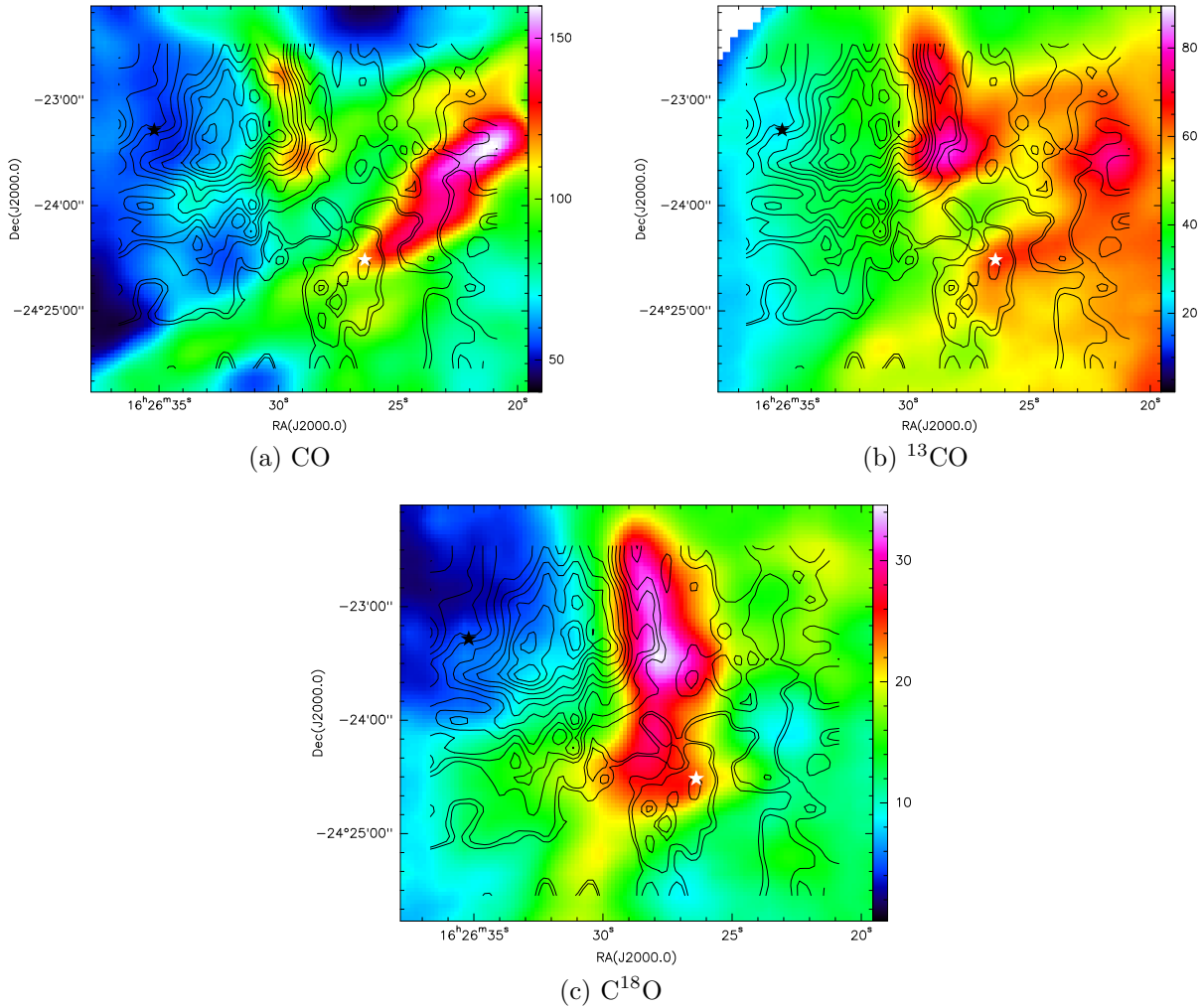
Figure 3.3: Integrated emission of J=3-2 transition of CO and its isotopologues for the region, for velocity 0-7 km/s. [CII] 158 μm emission is shown in black contours, for comparison. The star S1 is shown by black star, and the protostar VLA1623 is shown as red mark.

11

It is immediately clear that the distribution of CO is very different from that of C^+. The emission is much more extended, unlike the [CII] map. One local peak in intensity is observed, for all three tracers, at the west edge of the S1 PDR. This emission is from the denser molecular cloud outside the PDR. For CO and ^{13}CO, another component is seen near the protostar VLA1623. The emission near VLA1623 can be associated with the molecular outflow from the protostar. The rarer isotopes of CO trace a higher density in the molecular cloud. From the maps of CO, ^{13}CO and C^{18}O, it is easily seen that the location of the peak intensity in emission moves further from the PDR and deeper in the molecular cloud, as we switch to rarer isotopologues.

(a) CO

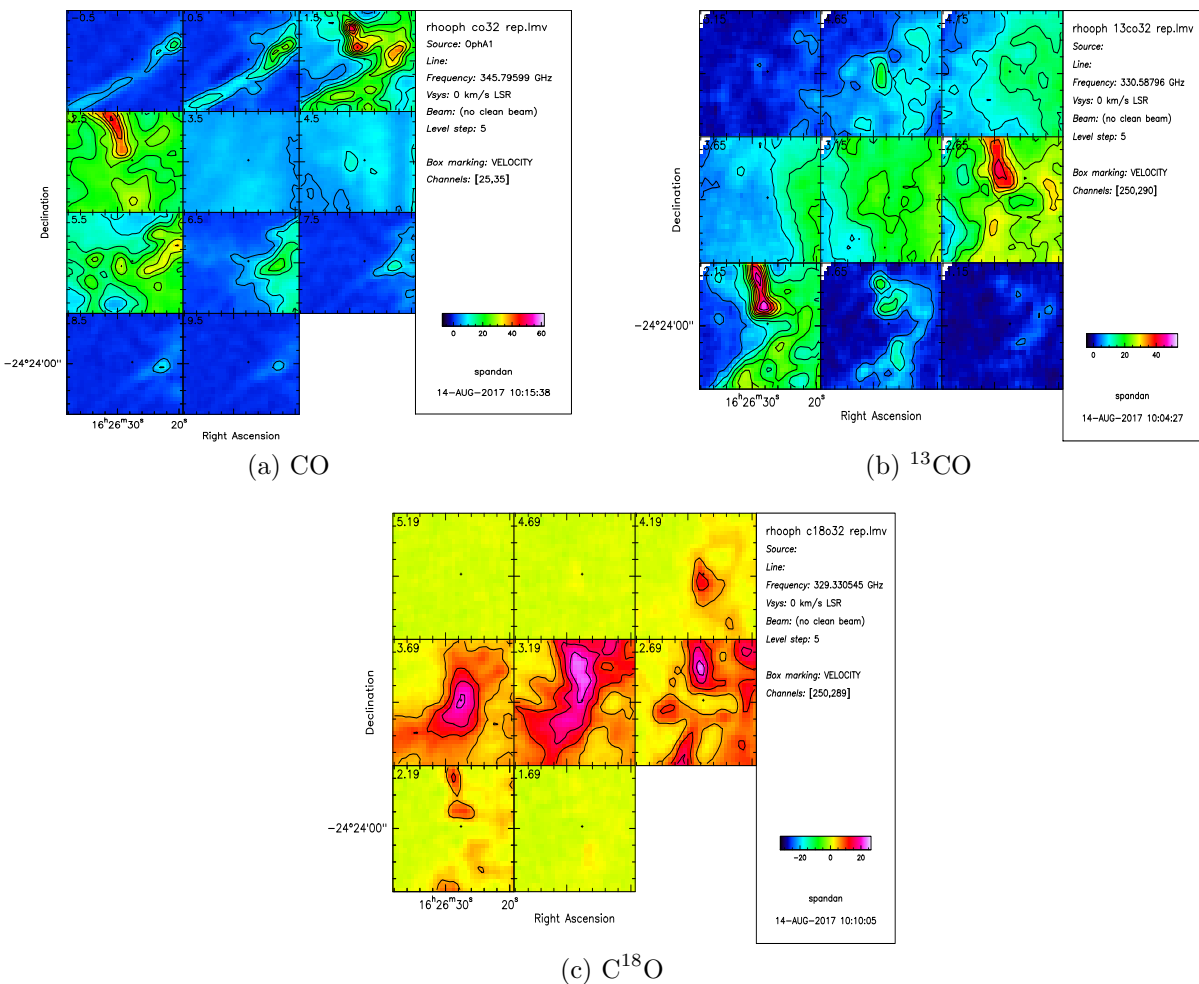

(b) ^{13}CO

(c) C^{18}O

Figure 3.4: Channel maps of CO and its isotopologues for the region. Each panel corresponds 1 km/s in the CO map, and 0.5 km/s in the other two. Other details are same as Figure 3.2

In order to determine the contribution from the molecular cloud and the outflow, it is

12

essential to separate the components. In Figure 3.4, we show the velocity maps for CO, ^{13}CO and C^{18}O. For CO, we clearly see different components, separated both spatially, and in velocity. Three components can be seen : at $v \sim 0$, 2 and 5.5 km/s. In case of ^{13}CO, we can still see emission at these velocities, spatially separated, but here, the separation is not very clear in velocity. Finally, for the rarest isotopolouge, C^{18}O, we see only one component, around the LSR velocity. This could be explained by absorption of CO by a cold cloud in the line of sight, which leaves the much rarer C^{18}O unaffected. We further look at the detailed spectra for these different tracers, and discuss in Section 4.2.

3.2.3   [OI] 63 μm and 145 μm

Figure 3.5 shows the intensity of two transitions in neutral oxygen, [OI] at 63 μm, and at 145 μm. [OI] maps are known PDR tracers, and are widely used in the studies of PDRs. The lines have a higher critical density, at $\sim 10^5$, and hence, trace a denser region. Both the maps, presented in Figure 3.5 cover a slightly smaller area than the other tracers.

(a) [OI] 63 μm   (b) [OI] 145 μm
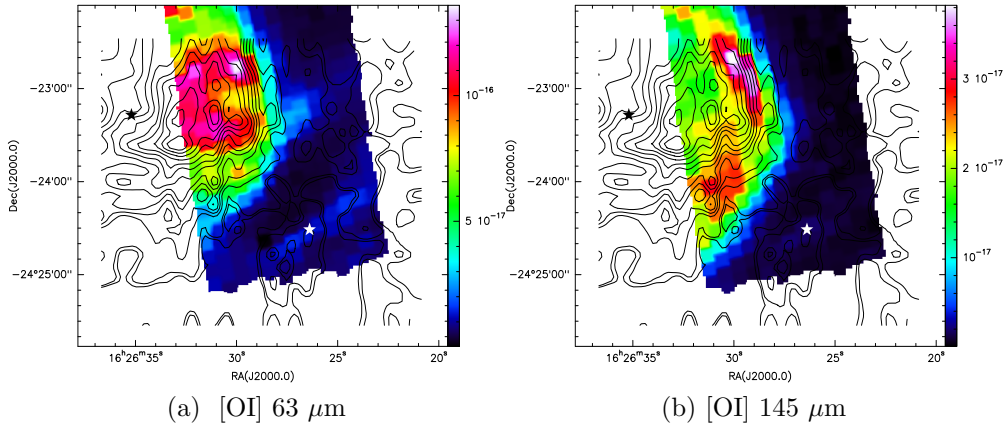
Figure 3.5: Observation of neutral oxygen in ρ Oph A. The black and white stars show the positions of the star S1, and the protostar VLA1623, respectively. [CII] 158 μm emission is shown in black contours, for comparison.

[OI] emission is seen to be predominantly originated from the gas next to the illuminating source, S1. Comparison with the [CII] map shows that these two maps share roughly the same boundary. The [OI] emission at 63 μm, for transition ^{3}P$_1$-^{3}P$_2$, is observed to be peaked deeper inside the ρ Oph PDR. The emission at 145 μm, corresponding to transition ^{3}P$_0$-^{3}P$_1$ peakes towards the boundary of the PDR, away from the illuminating source. The VLA1623

outflow can be faintly noticed towards the south in the [OI] maps.

Since the [OI] lines are not resolved in velocity in these observations, it is not possible to directly determine if the lines are self-absorbed. Indirect methods have been employed to answer this, such as mapping the ratio of intensities of the two lines. From the flux ratios of the two [OI] lines , it has been concluded that [OI] 63 μm is likely self-absorbed by a foreground cold cloud, whereas the higher level 145 μm line is unaffected. (Larsson & Liseau, 2017 [27])

3.2.4 Dust Continuum

Continuum emission in the infrared wavelength is the dominant pathway for cooling of the dust grains. So, continuum maps in the IR show the distribution of hot dust in the region. We use continuum observations at two wavelengths, 8 μm and 70 μm. In particular, the 8 μm emission is associated with the transient emissions from polycyclic aromatic hydrocarbons(PAH). The PAH molecules, like neutral oxygen, are also dedicated PDR tracers, which has been used widely before. (Croiset et al.(2016) [9], Jensen et al.(2017) [23])

(a) 8 μm continuum

(b) 70 μm continuum
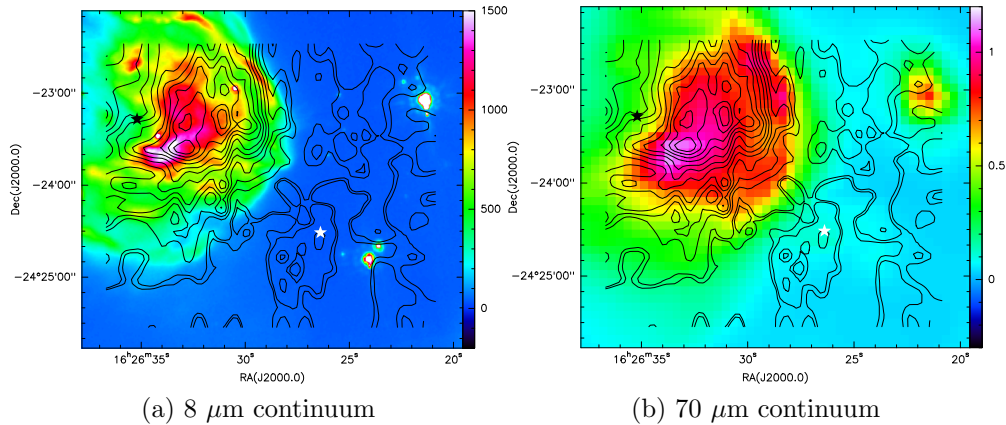
Figure 3.6: Infrared continuum maps showing the dust emission. The black and white stars show the positions of the star S1, and the protostar VLA1623, respectively. For comparison, [CII] 158 μm emission is shown in black contours.

Both the maps indicate that presence of hot dust is limited mostly inside the boundary of the hot, low density region mapped by [CII]. The 70 μm map shows a fairly homogeneous map, whereas the PAH emission at 8 μm appears to be much more inhomogeneous.

Chapter 4

Discussion on Observations

4.1   Comparison between different tracers

In this section, we look at the maps for different tracers, and compare the their distribution. For this purpose, in Figure 4.1, we show maps of ^{13}CO, [OI] 63 μm and PAH emission in 8 μm continuum.
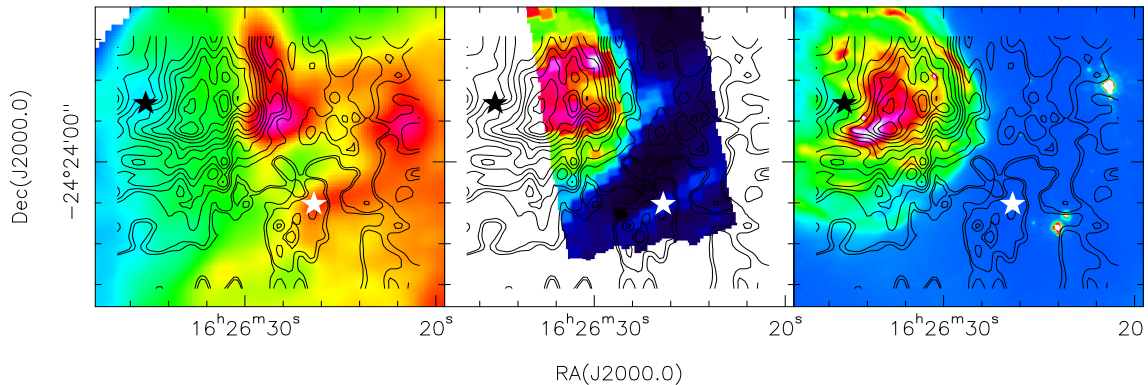
Figure 4.1: from left to right : maps of integrated ^{13}CO emission between 0 km/s and 7 km/s, [OI] 63 μm and continuum emission at 8 μm in the region. The black contours show [CII] emission. The black star show the position of S1, and the white star shows VLA1623.

We see that the PDR tracers, [CII], [OI] and PAH emission, all originate from the same region, and are confined to roughly the same boundary. These emissions are inhomogeneous, and originate from the same widespread low-density carbon region. Since the [OI] lines have

high critical density, the emission of these lines from the low-density region indicate clump-like structures inside the PDR. By contrast, the CO emission is observed to originate from the denser molecular gas outside the PDR, and have little overlap with the C^+ region.

From the [OI] and the dust continuum maps, we see a clear boundary of the PDR. The boundary is in the shape of a spherical shell around the star S1, and lies < 0.1 pc ($\sim 1.75'$ in the maps) from it. This boundary agrees with the boundary from H_2 pure rotational lines, presented in Larsson & Liseau, 2017 [27].

Although we do not see much emission in CO inside the PDR, this does not necessarily indicate low abundance of CO in the region. The low intensity observed might be down to the fact that the region inside the PDR is fairly hot, and that we are looking at a low-J transition for the molecule. For high incident radiation and corresponding high temperature, we might need to look at mid-J or high-J transitions to better observe CO in the region.

4.2 Analysis of C^+ and CO Spectra

In case of absorption by a foreground cloud, the absorbing cloud, being at a lower temperature, has a smaller Doppler broadening. Thus, the absorbed spectra will have a narrower profile, compared to the emitted spectra. If a tracer is indeed absorbed by a foreground cold cloud, we therefore expect to see a dip in it intensity near the LSR velocity.
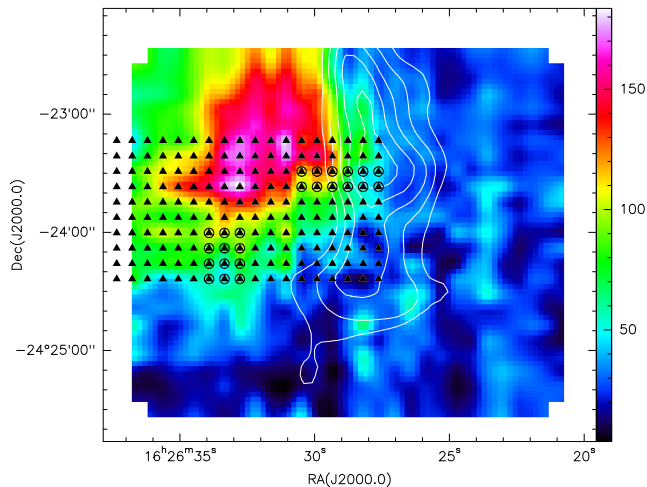

Figure 4.2: Selected positions for the spectra, shown in Figure 4.3. The triangles marked by an extra circle shows positions, where even the rarer $C^{18}O$ is absorbed by a foreground cloud. The colour map is of [CII], and the white contours show $C^{18}O$ emission.

In Figure 4.3, we show the spectra for [CII], CO and its isotopologues, for a few selected positions. The selected positions are shown in Figure 4.2. The entire sample is 180 points in a 18×10 grid. Each panel in Figure 4.3 shows spectra averaged for a 3×2 grid, staring from the north-east corner of the bigger sample.

From Figure 4.3, we see that, for most of the positions, [CII], CO and ^{13}CO show two peaks, on either side of LSR velociy of 2-4 km/s. Only C^{18}O, the rarest CO isotopologue, show only one peak, at v_{lsr}. This implies that, for most of the positions selected here, the tracers, except for C^{18}O are absorbed by a foreground cold cloud. It can be also seen that in 2-3 of the panels, even C^{18}O appear to be very slightly absorbed by a foreground cloud. We have shown the positions, where C^{18}O shows this absorption, in Figure 4.2. One of the patches lie close to the C^{18}O peak.
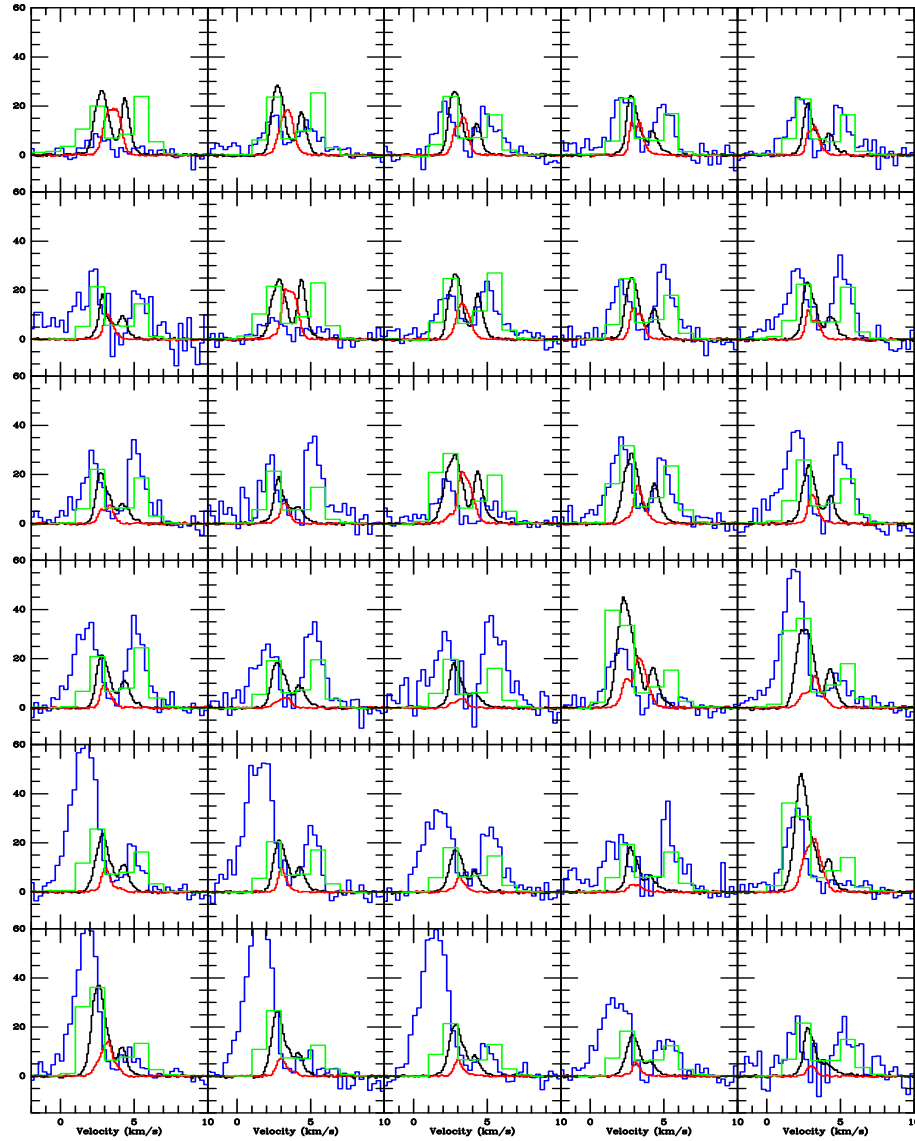
Figure 4.3: Spectra of [CII] 158 μm (blue) and J=3-2 transitions of CO (green), ^{13}CO (black) and C^{18}O (red). The spectra are for positions inside a rectangular patch considered, shown in Figure 4.2.

Chapter 5

The Meudon PDR Code

Numerical codes for PDRs are used to model clouds over a wide range of physical conditions, for different environments. The results from these models are used to interpret the observed data, mostly in the far-infrared, millimeter and submillimeter wavelengths, and relate the observed line intensities to physical parameters such as density and incident FUV flux. The PDR models use updated values of atomic and molecular data, chemical reaction rate parameters, and treatment of grain heating rates[24]. In this project, the PDR model we used is the Meudon PDR code (Le Petit et al. 2006 [29], http://ism.obspm.fr), available online, which is an updated version of the model of Le Bourlot et al, 1993 [28]. We have used the latest updated version of the code (June, 2017, version PDR 1.5.2 rev 1787).

5.1   Structure of the Code

The model considers a stationary cloud of gas and dust in a 1D parallel slab geometry. The cloud is illuminated by UV radiation from one, or both sides. At each position inside the cloud, the model solves for the radiative transfer, chemistry and thermal balance, by iteration. For each iteration, quantities such as temperature, heating and cooling rates, chemical reactions and abundances of chemical species, etc., are computed for each position. Finally, the code computes the column densities of species (and at different levels of excitation) and the intensities of line and continuum emission for the cloud. The desired quantities can be extracted with the help of python-based tools that are provided along with the code.

For computation, the 1D cloud of gas and dust is divided into slabs, the number of which depends on the total visual extinction considered. At each position in the cloud, the code solves for global radiative transfer for fixed local state, and then for the temperature, excitation and chemistry at the position, for the radiation field. This process is repeated for 10 iterations or more, depending on reaching of convergence(which can be checked from the results). The local state (chemistry, thermal balance and excitation) are solved alternatively. The code structure can be summarised as follows(Bron, thesis, 2014 [2]) :

- Loop over positions
  - Loop for local convergence
    * Excitation equilibrium
    * Chemical balance
    * Thermal Balance
  - Global radiative transfer

5.1.1 Radiative Transfer

At each depth, τ_v, the code solves for radiative transfer in UV, considering continuum absorption by dust, and discrete absorption, corresponding to transitions in H and H_2. Calculations are performed for photo-ionisation of C and S, photo-dissociation of H_2 and HD; and predissociating lines of CO. The 1D radiative transfer equation is given by (Gonzalez Garcia et al., 2008 [19]) :

$$\mu\frac{\delta I_\nu}{\delta\tau_V} = (a_\nu^D + E_{ij}(x_j - x_i)I_\nu)I_\nu - D_{ij}x_i I_\nu - a_\nu^D I_\nu^D \tag{5.1}$$

Here, I_ν is the specific intensity in the direction given by $\mu = cos\theta$, and $\tau_V = 2.5log_{10}(e)A_V$ is the opacity. $a_\nu^D = \frac{\kappa_\nu^D}{A_V}(2.5log_{10}(e))$, where κ_ν^D is dust absorption coefficient, and I_ν^D is the dust emissivity. $E_{ij} = (\frac{\lambda_{ij}^2}{8\pi})\frac{n_H}{A_V}g_i A_{ij}$, where A_{ij}'s are Einstein coefficients, and g_i's are statistical weights for the ith state. The line profile is given by I_ν. $x_i = \frac{n_i}{g_i n_H}$, and $D_{ij} = (\frac{n_H}{A_V})(\frac{h\nu_{ij}}{4\pi})g_i A_{ij}$.

Dust properties are taken from Laor and Draine, 1993 [26], and the dust scattering is solved for by Henyey-Greestein approximation (Henyey and Greenstein, 1941 [20]). For a number

of chemical species, the number of levels to be considered can be chosen(limitation being consideration of more lines increase the computing time). For other lines, the FGK approximation for self-shielding is used (Federman, Glassgold, and Kwan, 1979 [13]).

5.1.2 Thermal and Chemical Balance

To solve for temperature and abundances of species, the energy and chemical equilibrium has to be solved simultaneously. At a point at depth z, the energy balance is given by (Tielens and Hollenbach, 1985a [49]) :

$$\Sigma_i \Gamma_i(T(z), x(z)) - \Sigma_j \Lambda_j(T(z), x(z)) = 0 \tag{5.2}$$

Where, Γ_i and Λ_i are different heating and cooling terms considered. x(z) represents abundances at depth z. In a PDR, the primary heating mechanism is photo-electric heating by the FUV photons on the dust grains. For this process, the code follows updated treatment from Weingartner and Draine, 2001(b [53],c [54]) and Weingartner et al., 2006 [55]. The other major heating pathways are photo-ionisation and photo-dissociation of different species, exothermic reactions and ionisation by cosmic rays. The Meudon PDR code explicitly considers the formation of H_2 on dust grains, which is a major heating mechanism. For H_2 formation, the distribution used is from Sizun et al., 2010 [48]. The cooling is mostly through atomic and molecular transitions, the dominant lines being those of C^+, O and CO. Transitions are considered in the code for all species, whose excitation is computed. Contribution of gas-grain collisions is taken from to Burke and Hollenbach, 1983 [3].
In steady state, the chemical abundances of all species are solved using :

$$F(T(z), x(z)) = \frac{dx(z)}{dt} = 0, \tag{5.3}$$

The chemical species and reactions to be considered can be chosen appropriately. The code includes ~ 150 species and ~ 3000 reactions, by default. The chemical network is built from a compilation of the databases UMIST, OSU (by Eric Herbst) and KIDA, along with a number of individual references. Apart from possible three body reactions, with two H-atoms, the elementary reactions considered are mostly two-body processes [29]. The chemical balance is solved for each specie, at each position, using Newton-Raphson method. Solving

21

equations 5.2 and 5.3 in iterative way, the code converges on solutions for abundances and the temperature at a point.

The Meudon PDR code applies steady state approximation in its calculations. This can be viewed as a drawback of using the code to compare with observations, specially of fast-changing clouds. For most of the radiation field strengths and densities used in the models, however, the timescales are moderate, and the time dependent effects do not dominate. Thus, for most of the used cases, steady state approximation holds.

5.2   Values of parameters used in the models

The number of global iterations is chosen by the user, considering computation time and convergence of parameters. The cloud can be set to be illuminated by radiation field from nearby star and/or the interstellar radiation field(ISRF); from one, or both sides. The size of the cloud is controlled by specifying the total visual extinction. The code can be run for constant density or constant pressure models (pre-defined profile in density or pressure, and temperature can also be used). Properties of grains, metallicity and other small parameters can be changed from the default values.

In this project, the Meudon PDR Code was used with the objective to study the effects of density, incident FUV flux and metallicity on observed intensities of different lines emitted from the cloud. Therefore, for most other parameters to be provided as input for the code, the values were kept unchanged from the default values in the downloaded version.

The code was run for a grid of values of number density and radiation field to model dense cloud, illuminated in a young stellar environment. The total visual extinction was chosen to be 7. The number densities used were $n_H(\mathrm{cm}^{-3}) = 10^3, 10^4, 10^5, 10^6, 10^7$. We chose the modeled clouds to be illuminated from one side, for a range of radiation field strength. We have used the Mathis prescription of FUV radiation field intensity, based on Mathis et al., 1983 [35], and Black, 1994 [1]. The expression used to estimate this field in the code is (for $\lambda \leq 8000$ Å) :

$$I(\lambda) = [\tanh(4.07 \times 10^{-3} \times \lambda - 4.5991) + 1.0] \times 107.192 \times \lambda^{-2.89} \tag{5.4}$$

Here, intensity, I is in units ergs $cm^{-2}s^{-1}$ $\mathring{A}^{-1}sr^{-1}$ and wavelength, λ is in Å.This approximation correspond to a radiation field intensity of 6.42×10^{-14}ergs cm^{-3}, integrated for wavelength 912 to 2400 Å. In the same range, the Habing radiation field has strength 6.21×10^{-14}ergs cm^{-3}. Since the field strength is very close to the Habing field for the range, we will denote the FUV field in this project by G_0. In the near-UV, optical and near-IR wavelengths, the radiation field is modelled by black-body radiation field from three bodies at at 6184, 6123 and 2539 K. The cosmic microwave background(CMB) radiation is also taken into account, by considering a radiating body at 2.73 K. The infrared component is assumed to be from dust emission, and is computed by the DustEM code (developed by Institut d'Astrophysique Spatiale and Institut de Recherche en Astrophysique et Plantologie, website : http://www.ias.u-psud.fr/DUSTEM/).

The multipliers of radiation field strength used are $G_0 = 10, 50, 10^2, 5\times10^2, 10^3, 5\times10^3, 10^4, 10^6$. This whole grid of models were run for metallicities of 0.5, 1.0 and 1.9 times solar standard.

For simplicity of analysing, we have used constant density models for all the runs. After trying out different limits for the number of global iterations, it was found that the desired quantities, such as densities of important species(C, C$^+$, H, CO and O) converged for iterations ≥ 7. To ensure convergence, all the models were run for 10 iterations. Parameters deciding cosmic ray inonisation rate and grain properties were kept unchanged from the default values provided in code for galactic environment. Default values are adopted for H$_2$ formation, excitation and collision rates, and turbulent velocity, as well. List of all important parameters used can be found in Table 5.1. The abundance of chemical species and the network of chemical reactions and excitation were also kept unchanged from the default values give. Some of the important gas-phase abundances can be found in Table 5.2. For solving UV radiative transfer, we have opted for using the FGK approximation(from Federman, Glassgold and Kwan, 1979 [13]) over treating the exact transfer(described in Goicoechea & Le Bourlot, 2007 [16]) to reduce the computing time. The difference in results from the two methods is not significant for dark, dense clouds, which we have modeled on in this project. The exact method is more important in studying distribution of H/H$_2$, whereas, in our case, we have focused on distribution of C, O and CO (and its isotopologues). Thus, using FGK approximation does not affect the output significantly, but cuts down the computing time.

Table 5.1: Summary of Important Model Parameters

Parameter	Value(s) Adopted	Comment/Description
$n_H(\text{cm}^{-3})$	$10^3, 10^4, 10^5, 10^6, 10^7$	$n_H = n(\text{H}) + n(\text{H}^+) + n(\text{H}_2)$
χ (front side)	$10, 50, 10^2, 5 \times 10^2,$ $10^3, 5 \times 10^3, 10^4, 10^6$	In units of Mathis Radiation field
χ (back side)	0.00	
Number of iterations	10	
A_V	7	Visual Extinction
Cosmic Ray ionisation rate	5×10^{-17} s^{-1}	Number of H$_2$ molecules ionised per sec
Turbulent Velocity	$2\ km\text{s}^{-1}$	Determines Doppler broadening. Value typical for galactic regions.
$R_v = A_V/E(B-V)$	3.10	Total to selective extinction ratio
Metallicity, Z	0.5, 1.0, 1.9	
Dust to gas mass ratio	0.01	Value multiplied by metallicity in code
PAH/dust (mass ratio)	0.00	
Grain distribution	MRN power law	Reference : Mathis, Rumpl and Nordsieck, 1977 [36]

Table 5.2: Used Gas Phase Abundances for Some Important Species

Chemical Specie	Initial Abundance Relative to n_H	Comment
H$^+$	0.0	None of the Hydrogen is present
H	0.8	in the form of H$^+$, as PDRs
H$_2$	0.1	lie outside the ionised region
He	0.1	
C$^+$	1.339 $\times 10^{-4}$	All carbon is assumed to be
C	0.0	in singly ionised state;
CO	0.0	^{12}C : ^{13}C ≈ 68
O	3.196 $\times 10^{-4}$	
N	7.5 $\times 10^{-5}$	
S	1.86 $\times 10^{-5}$	
Si	8.2 $\times 10^{-7}$	Present entirely in singly ionised state
Fe	1.5 $\times 10^{-8}$	

Chapter 6

Effect of Density, Incident FUV Radiation Strength and Metallicity on Line Intensities from PDRs

The Meudon PDR code was used to model clouds at solar metallicity with different initial density and incident FUV flux, with the objective to study the effect of these two parameters on the distribution of gas in the cloud. Further, we ran the model on the grid also for metallicity values 0.5 and 1.9 times solar, to study the effect of metallicity on PDR properties. The results are discussed in the following sections.

6.1   Density Distribution inside the Cloud

In this section, we discuss the distribution of important elements, such as hydrogen, carbon and oxygen in the modelled clouds with respect to varying density and strength of the incident radiation field. Inside the PDR, hydrogen is present in both atomic and molecular form, and in trace amounts, singly ionised form. Carbon is expected to be present in singly ionised (C^+), neutral atomic (C) and in molecular form in CO. Oxygen is present in both atomic and molecular forms. In the following sections, we discuss the distribution of these species.

Although our grid of model spanned five values for $n_H(10^3 \ cm^{-3} - 10^7 \ cm^{-3})$ and eight

values for $G_0(10 - 10^6)$; due to the constraint of space, we show the plots corresponding to only three values each for n_H & G_0. To get a fair representation of the grid, we have picked either extremes, and a middle value, for each of these two parameters. Thus, in the sections 6.1.1, 6.1.2 and 6.1.3, we only show results for $n_H = 10^3, 10^5$ and 10^7 cm^{-3} and $G_0 = 10, 10^3, 10^6$.

6.1.1 Distribution of Hydrogen

Figure 6.1 shows the density distribution inside the cloud for H$^+$, H and H$_2$. It can be seen that atomic hydrogen dominates abundance for low visual extinction, whereas at high extinction($A_V \gtrsim 2$), the dominating species is H$_2$. H$^+$ is present in trace amounts, and falls sharply with A_V at $A_V \sim 1 - 2$. The density of H$^+$ is more than 4 orders of magnitude less than that of atomic or molecular hydrogen, for most part of the cloud.

(a) Distribution of atomic hydrogen (b) Distribution of H$_2$ (c) Distribution of H$^+$
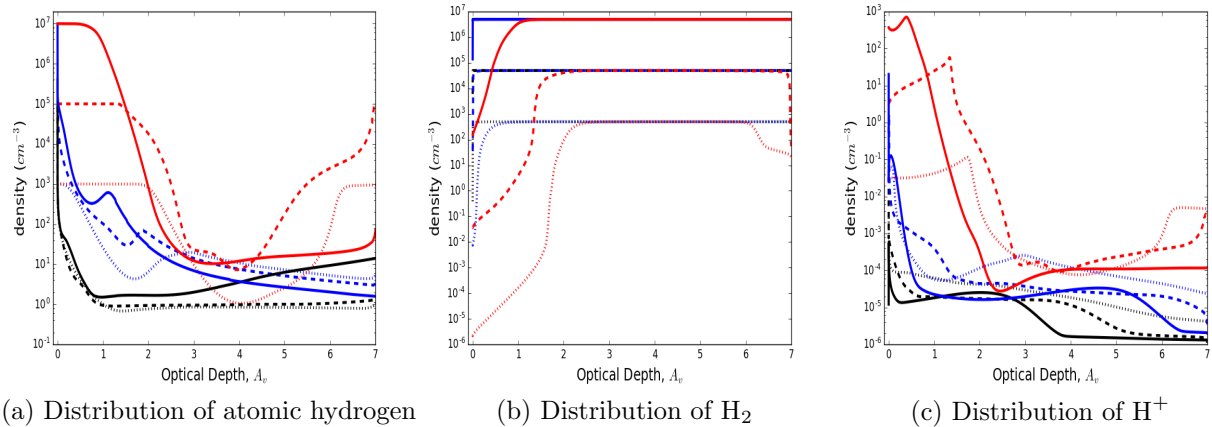
Figure 6.1: Density of different hydrogen-bearing species as a function visual extinction. The solid curves correspond to $n_H = 10^7$ cm^{-3}, the dashed curves, to $n_H = 10^5$ cm^{-3} and the dotted ones, for $n_H = 10^3$ cm^{-3}. The black curves are for $G_0 = 10$, the blue ones show $G_0 = 10^3$ and the red curves correspond to $G_0 = 10^6$.

The density of atomic hydrogen is maximum at the edge of the PDR, and falls off with A_V. How fast it decreases depends on the incident FUV flux. For higher G_0, the atomic region extends further into the cloud. This trend is evident from the curves for same number density, but varying G_0 in Figure 6.1(a). For the distribution of H$^+$, the trend is similar. The density of H$_2$ is low at the edge, and increases with A_V, and saturates after a point.

Saturation is reached faster for lower G_0. In Figure 6.1(b), this behaviour is most apparent for density of 10^3 cm^{-3}. For both atomic and molecular hydrogen, the peak density is observed to be decided by the number density considered. For example, the dashed curves in Figure 6.1(a), corresponding to $n_H = 10^5$ cm^{-3}, show a density of $\sim 10^5$ cm^{-3} at $A_V = 0$; meaning that at the edge, nearly all the hydrogen is present in the atomic form. At high extinction, most of the hydrogen is present in the form of H_2.

At the edge of the cloud, the shielding is minimum, and the radiation strength is highest. Thus, the peak density of both H and H^+ is seen very close to, or exactly at, the edge. As we go deeper into the cloud, due to increased shielding, the photodissociation of hydrogen molecule ceases, resulting in decrease in density of H and increase in that of H_2. Increase in the number density results in better self-shielding of the radiation, and hence the H_2 peak is reached sooner. This is best seen from the $G_0 = 10^6$ curves in Figure 6.1(b). Also, increase in the FUV radiation strength means than that there is better penetration of the radiation into the cloud. Hence, for higher G_0, the photodissociated, ie., the atomic region extends further into the cloud. The atomic region extends upto $A_V \sim 1 - 2$, and deeper inside, H_2 is the more abundant specie.

6.1.2   Distribution of Carbon-bearing Species

Inside a PDR, the primary species containing carbon are C^+, C and CO. Figure 6.2 show the density of these three species with visual extinction. Distribution of these species follow roughly same trends of H and H_2, discussed in the Section 6.1.1. The most abundant specie changes from C^+ to C, and then to CO, starting from the edge of the cloud.

The FUV photons (6eV $< h\nu < $ 13.6eV) have enough energy to ionise carbon (ionisation energy $\sim 11.26eV$). Thus, at the edge, where there is little to no shielding, most of the carbon is present in ionised form. Deeper into the cloud, the photons are not energetic enough to ionise carbon, and hence, density of C^+ falls with A_V. For moderate extinction, the radiation can still dissociate CO. Penetration of the radiation is more for lower density and higher incident flux. This results in extension of the C^+ and atomic carbon regions and C^+/C and C/CO transition layers shift deeper. Deep inside the cloud, radiation is not energetic enough to dissociate CO, and its density saturates at high A_V. The saturation is reached sooner for higher n_H and lower G_0. The maximum density for all three species is decided by the number density. In Figure 6.2, we do not see saturation for $n_H = 10^3$ cm$^{-3}, G_0 = 10^6$,

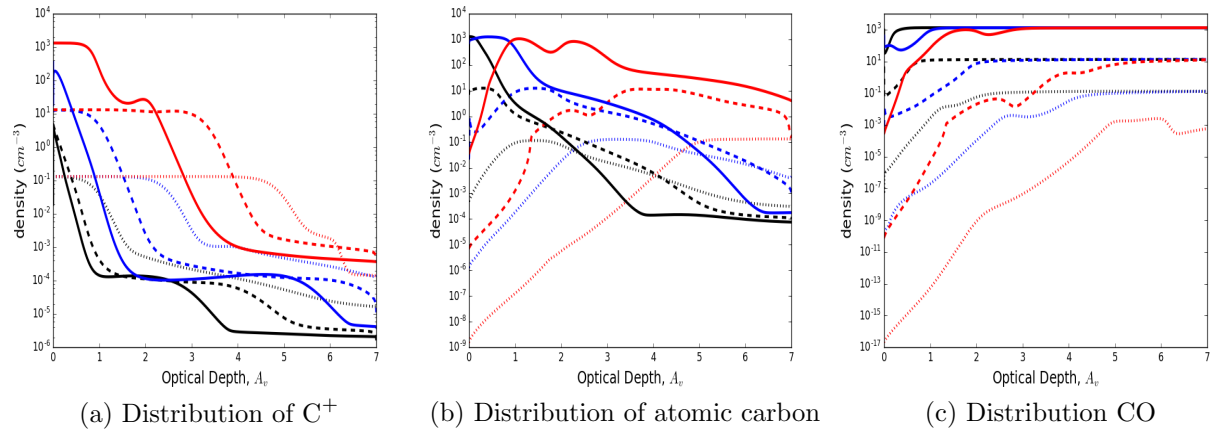(a) Distribution of C$^+$ (b) Distribution of atomic carbon   (c) Distribution CO

Figure 6.2: Density of different carbon-bearing species as a function visual extinction. The color and style coding of the graphs are same as in Figure 6.1

suggesting that an optical depth more than $A_V = 7$(which was considered in the models) is needed for it. The trends with density and FUV radiation strength are seen best from curves for $n_H = 10^3$ cm^{-3}, and $G_0 = 10^6$, respectively, in Figure 6.2.

The atomic region(where hydrogen is mostly in atomic form) extends only upto $A_V \sim 1 - 2$, whereas carbon is found in ionised and atomic form upto $A_V \sim 5$, specially in low-density and high-illumination clouds. In these regions, CO, which is widely used as a tracer for the molecular gas, shows very weak emission (Wolfire et al., 2010 [57]). This effect is enhanced in low-metallicity observations [22]. Therefore, for such 'CO-dark gas', other tracers need to be used in observations. C$^+$ is one such useful tracer.

6.1.3   Distribution of Oxygen

The distribution of atomic and molecular oxygen is shown in Figure 6.3. It can be seen that most of the oxygen is present in atomic form throughout the cloud, and density of molecular oxygen is lower by about a factor of 10^4 or more inside. The density of both atomic and molecular oxygen does not vary much with change in incident radiation strength, and is largely dependent on the density of the cloud. This behaviour is most clearly seen in Figure 6.3(a).

In a PDR, the transition from atomic to molecular oxygen takes place at $A_V \sim 10$. Since
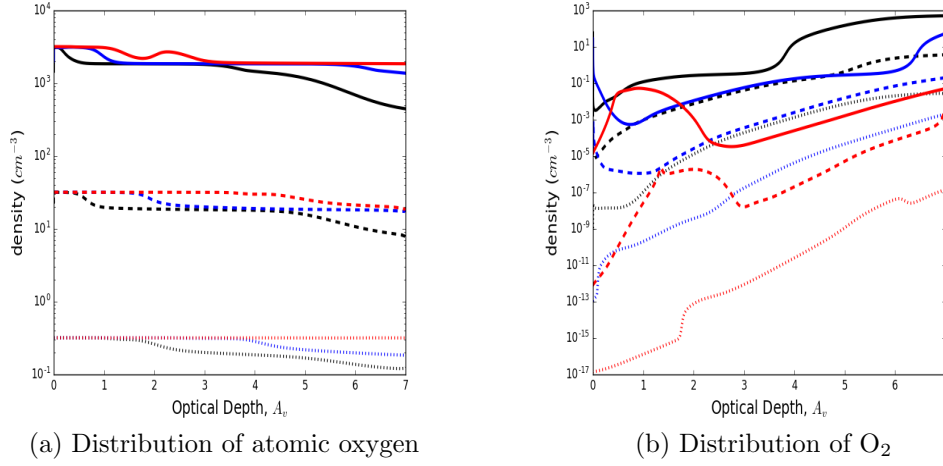
Figure 6.3: Density of atomic and molecular oxygen as a function visual extinction. The color and style coding of the graphs are same as in Figure 6.1

our modeled clouds have visual extinction only upto $A_V = 7$, we do not see this transition in the results. For the depth of the cloud considered, most of the oxygen is present in atomic form, and the amount of O_2 is very small.

It is worth noting that the observations of O_2 has proven to be very difficult. Goldsmith et. al., 2000 [18] report a mean O_2 abundance of 0.33×10^{-7}, relative to H_2 for 20 galactic molecular clouds, observed with the Submillimeter Wave Astronomy Satellite(SWAS). For the H_2 peak position in Orion, the abundance is found to be $(0.3 - 7.3) \times 10^{-6}$ (Goldsmith et al., 2011 [17]), and for ρ Oph A, this value is reported to be as low as 5×10^{-8} (Liseau et al., 2012 [32]). These abundances are much lower than what is predicted for moderately dense molecular clouds. The predicted values from Figure 6.3 does, in fact show a fractional abundance of $\sim 10^{-6}$ for O_2 relative to H_2 (which agrees with the observed abundances), but as mentioned before, since we have only considered models for optical depth less than the transition region for atomic to molecular oxygen, it is highly likely that our models do not show much of the molecular oxygen in the cloud. Therefore, we looked at pre-computed PDR models from the online Meudon PDR database(http://ismdb.obspm.fr/), which are generated using the same version of the Meudon PDR Code, that we have used in our project. We looked at models with higher optical depth ($A_V = 20$ and $A_V = 30$) than what we had considered. These models predict $N(O_2)/N(H_2) \sim 10^{-4}$, for moderate-to-high density ($n_H \geq 10^4 \text{cm}^{-3}$) and $G_0 = 1 - 10^4$. Thus, we see that, the abundances of O_2, derived from observations of different molecular clouds, is much lower than what is predicted from

models, by a factor of more than 100-1000. In observations of molecular clouds, O_2 has been highly elusive, and remains an open problem in sub-mm astronomy.

6.2   Line Intensities

In this section, we show the intensities and ratios of strength for a few important transitions of H_2, [CII], [CI], CO and [OI]. C^+ and neutral oxygen are present mostly inside PDRs, and hence, exclusively traces PDR regions. The H_2 ro-vibrational lines are observed in high temperature regions, where the molecules are collisionally excited. Neutral gas near star forming regions is an excellent source of H_2 rovib transitions.

We present isocontour plots for intensity and line ratio over the entire range of input parameters $n_H(10^3$ cm^{-3} - 10^7 cm^{-3}) and $G_0(10$ - 10^6). Later, to observe the trends better, specially at high G_0, we also added three more values of n_H (2×10^5 cm^{-3}, 5×10^5 cm^{-3} and 7×10^5 cm^{-3}) and eight more values of G_0 ($2.5 \times 10^4, 5 \times 10^4, 7.5 \times 10^4, 2.5 \times 10^5, 5 \times 10^5, 7.5 \times 10^5, 2.5 \times 10^6$ and 5×10^6), and ran the models on this extended grid. The intensities of the transitions are computed in units ergs cm^{-2}s^{-1}sr^{-1}, and with the assumption that the PDR is viewed face-on, ie., the emission is from the side towards the incident radiation. In Section 6.2.1, we present results for few H_2 rovib transitions, in Section 6.2.2; results for important far-infrared lines [CII] 158 μm, [OI] 63 μm and 145 μm; and in Section 6.2.3, cooling lines for neutral carbon and some important CO rotational transitions.
We have also compared our model plots with previous results from Kaufman et al., 1999 [24] and Le Petit et al., 2006 [29]. The results are in very good agreement, with the exception of the ratio of intensity of [OI] 145 μm to that of [OI] 63 μm.

6.2.1 H_2 Quadruple Transitions

The H_2 ro-vibrational transitions indicate temperatures in the excess of 1000 K (Table 6.1). In regions of $T = 10^3 - 10^4$ K, these can be the dominant cooling lines, especially in low-metallicity regions.

In Figure 6.4, we show the intensity of 1-0 S(1) transition for H_2, as a function of density and incident radiation strength. This transition, at 2.12 μm, has been studied for a wide

Table 6.1: Line Data : H_2 Quadruple Transitions

Species	Transition	E_{ul}/k_B (K)
H_2	1-0 S(1)	6956
H_2	1-0 S(2)	7584
H_2	2-1 S(1)	12550
H_2	2-1 S(2)	13150
H_2	2-1 S(3)	13890

Energy levels are calculated from Dabrowski & Herzberg (1984) [10]

range of environments[29]. The intensity is sensitive to the radiation at low G_0, but at high G_0, it is sensitive more to density. In figures 6.5 through 6.9, we show the ratios of intensities of some of the transitions to the 1-0 S(1) intensity.
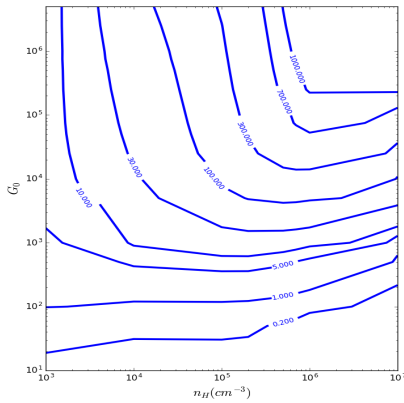
Figure 6.4: Intensity of transition 1-0 S(1) in H_2, in 10^{-6}ergs cm^{-2}s^{-1}sr^{-1}
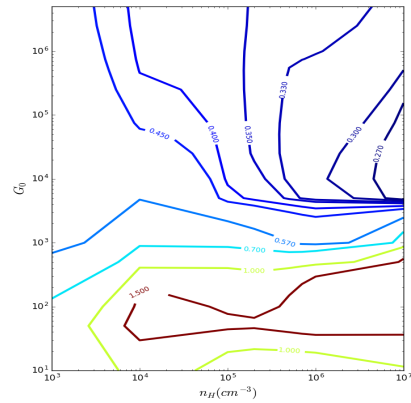
Figure 6.5: Ratio of intensities for the transitions 1-0 S(2) and 1-0 S(1) in H_2

From the results, it can be seen that these line ratios are dependent mostly on density for moderate to high G_0. At low G_0, the ratios(except $I_{H_2\ 2-1\ S(1)}/I_{H_2\ 1-0\ S(1)}$), are dependent on the strength of the incident radiation field. Thus, depending on the likelihood of the parameters, these ratios can be employed to determine density, or FUV flux in an observed region.
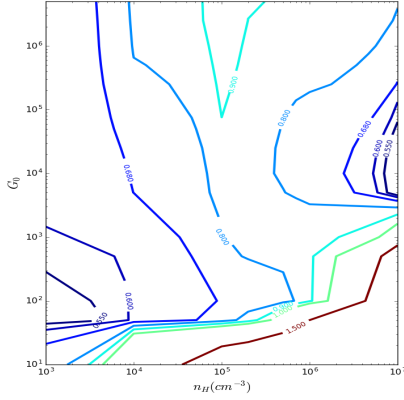
Figure 6.6: Ratio of intensities for the transitions 1-0 S(3) and 1-0 S(1) in H_2
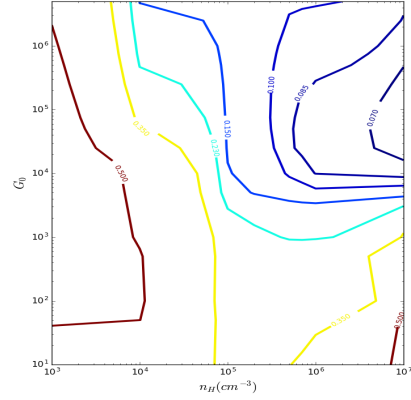
Figure 6.7: Ratio of intensities for the transitions 2-1 S(1) and 1-0 S(1) in H_2
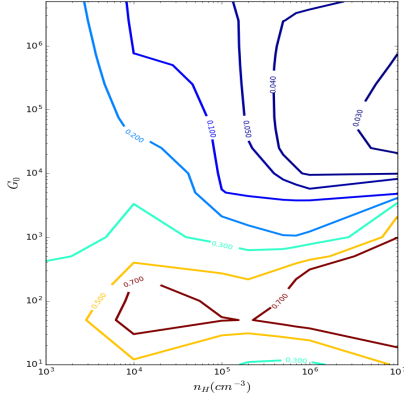
Figure 6.8: Ratio of intensities for the transitions 2-1 S(2) and 1-0 S(1) in H_2
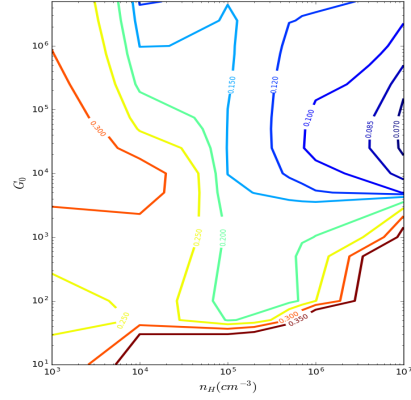
Figure 6.9: Ratio of intensities for the transitions 2-1 S(3) and 1-0 S(1) in H_2

6.2.2 [CII] 158 μm, [OI] 63 μm and 145 μm

Here, we present results for important FIR tracers [CII] at 158 μm, and [OI], at 63 μm and 145 μm. C^+ and neutral oxygen line emission is dominant cooling pathway for warm neutral medium. [OI] lines have a higher critical density, and hence trace denser region in the cloud.

Figure 6.10 shows the intensity of [CII] 158 μm line. The intensity is more sensitive to FUV flux, and decreases with increasing density. Figure 6.12 shows the ratio of the intensity of [OI] 63 μm line to that of [CII] 158 μm line. This ratio is highly sensitive to density,

Table 6.2: Table for Upper-level Energies and Critical Densities

Species	Transition	E_{ul}/k_B (K)	n_{cr} (cm^{-3})
[CII]	$^2P_{3/2}$ - $^2P_{1/2}$	92	3×10^3
[OI] 63 μm	$^3P_1$ - $^3P_2$	228	5×10^5
[OI] 145 μm	$^3P_0$ - $^3P_1$	326	1×10^5
[CI] 609 μm	$^3P_1$ - $^3P_0$	23.6	5×10^2
[CI] 370 μm	$^3P_2$ - $^3P_1$	62.5	3×10^3
CO	J = 2-1	16.59	1×10^4
CO	J = 3-2	33.19	5×10^4
CO	J = 4-3	55.32	1×10^5
CO	J = 6-5	116.16	4×10^5

Table adopted from Kaufman et al., 1999 [24]. Critical densities for [CII], [OI] and [CI] for collision with H, taken from Tielens & Hollenbach, 1985 [49]. Critical densities for CO for collision with H_2, and temperature of 100 K.

specially at higher densities, and can be used as an indicator of the density of an observed region. The sensitivity towards density can be understood in terms of difference in the critical densities of these two transitions. Critical density for [CII] 158 μm is $\sim 3 \times 10^3$, whereas for [OI] 63 μm is $\sim 5 \times 10^5$ (assuming collisional partner H; critical densities from Tielens and Hollenbach, 1985a [49]). In the range of densities we have considered, the density is almost always more than n_{cr} for [CII], so, the intensity does not increase rapidly with density. However, for the case of [OI] 63 μm, n_{cr} lies towards the end of the range, so, for most part, intensity of this transition increases fast with increasing density.

Ratio of intensities of [OI] lines at 145 μm and 63 μm is shown in Figure 6.11. For the parameter space presented in the plot, the ratio does not vary much. The critical densities for the two transitions being similar, the ratio is mostly insensitive to density[24]. In PDRs, the observed values are generally in the range 0.05-0.1 (Hollenbach and Tielens, 1999 [21]). In some regions, [OI] 63 μm line is optically thick, and the 145 μm line is optically thin. In those cases, the observed line ratios can be significantly higher. For example, due to foreground absorption of [OI] 63 μm in ρ Oph PDR, which leaves the 145 μm line unaffected, values near 0.17-0.5 are observed (Larsson and Liseau, 2017 [27]).
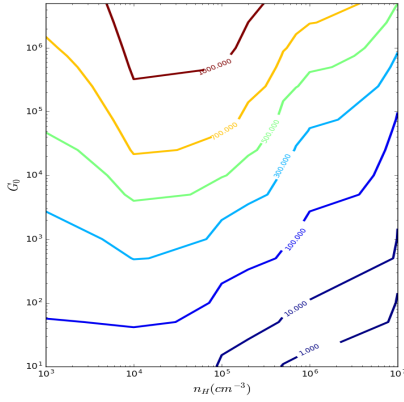
Figure 6.10: 1

58 μm]Intensity of [CII] 158 μm, in
10^{-6}ergs cm^{-2}s^{-1}sr^{-1}
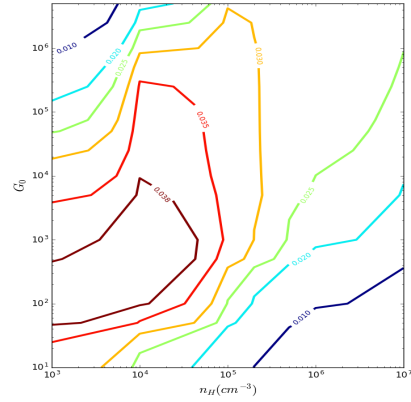

Figure 6.11: Ratio of intensities for the
[OI] lines 145 μm to 63 μm
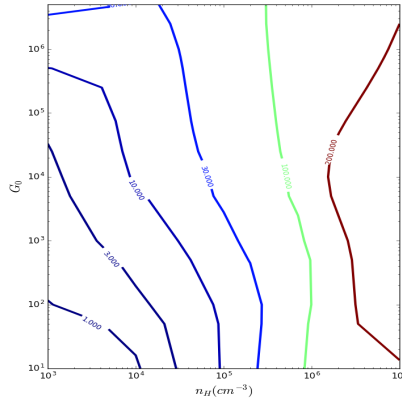
Figure 6.12: Ratio of intensity of [OI] 63
μm to the intensity of [CII] 158 μm

6.2.3 [CI] 370 μm and 609 μm, and CO Rotational Lines

In this part, we show intensities and line ratios for some important mm and sub-mm cooling
lines for neutral carbon and CO. These lines originates deeper into PDRs, where photo-
ionisation and photo-dissociation slows down, and carbon is found mostly in neutral form,
or in the form of CO. These lines are indicative of penetration of radiation into the cloud,
and of chemistry deeper inside. In the cold molecular gas, the dominant cooling lines are
CO transitions.
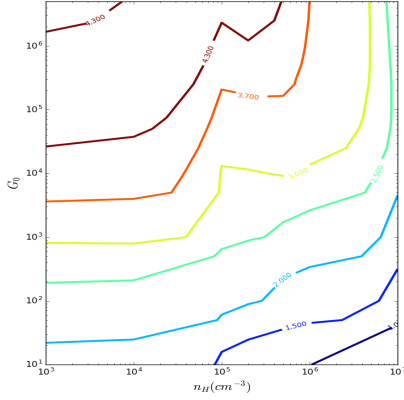
Figure 6.13: 6
09 μm]Intensity of [CI] 609 μm, in
10^{-6}ergs cm^{-2}s^{-1}sr^{-1}
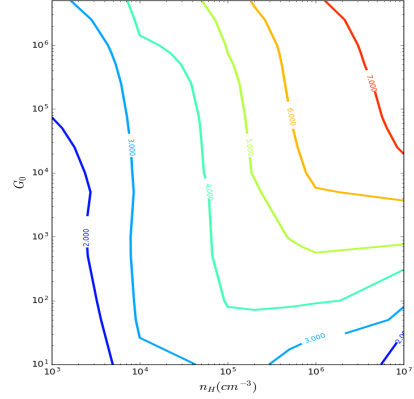
Figure 6.14: Ratio of intensities for the [CI] lines 370 μm to 609 μm
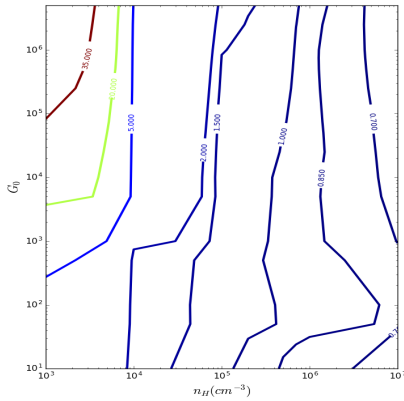
Figure 6.15: Ratio of intensity of the [CI] 609 μm line to the CO J=2-1 line
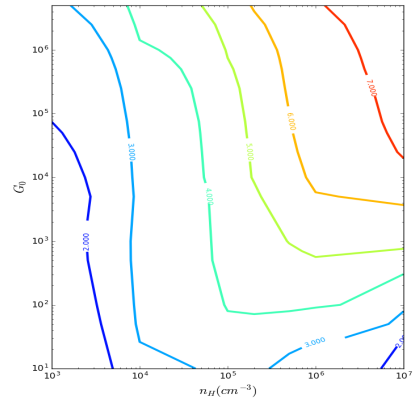
Figure 6.16: Ratio of intensity of the [CI] 609 μm line to the CO J=3-2 line

In Figure 6.13, intensity of [CI] 609 μm line is shown. It can be seen that the intensity does not change much in the parameter space considered. The column density of C is not sensitive to the strength of incident radiation field (Tielens and Hollenbach, 1985 [49]). Also, as the critical density of [CI] 609 μm transition is lower than the densities considered in our models, we do not see much change in the intensity of the line with density, as well. In fact, with increasing density, intensity of [CI] 609 μm line slowly decreases.

For similar reason, in Figure 6.14 the ratio of intensities of the [CI] lines at 370 μm and 609 μm does not vary much with density. The two transitions also have similar upper level energy, both of which are relatively low ($\sim$ 63 K and $\sim$ 24 K, respectively). Therefore, there

is not much dependence on G_0. Being emitted from the same species, the ratio of the two lines is not affected by abundance, either. We can see that over the entire range of n_H and G_0 considered, the ratio does not change by much.
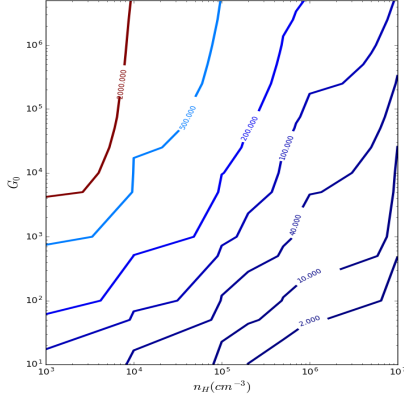

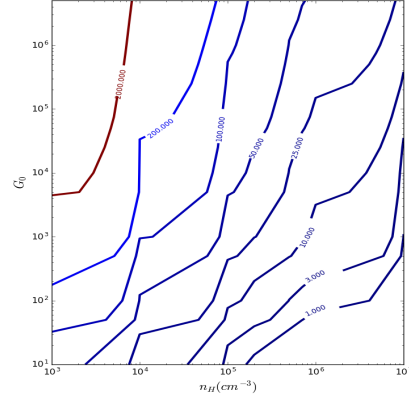Figure 6.17: Ratio of intensity of the [CII] 158 μm line to the CO J=2-1 line

Figure 6.18: Ratio of intensity of the [CI] 609 μm line to the CO J=3-2 line

Figure 6.17 and 6.18 show the ratios of intensities of [CII] 158 μm to that of CO lines J=2-1 and J=3-2. The [CII] and CO lines originate from different regions in a PDR. [CII] 158 μm line is produced near the surface of the cloud, whereas the CO lines arise from deeper in the molecular cloud. The ratios vary more with density. Due to the vast change in the ratio with n_H and G_0, this ratio can be used to determine density and radiation field in observed PDRs.

Ratio of intensity of [CI] 609 μm to that of CO J=2-1 and J=3-2 transitions are shown in Figure 6.15 and 6.16. These ratios are highly sensitive to density, specially for moderate to high G_0. Hence they can be used to determine density in observed regions.

Figures 6.19 and 6.20 show the intensities of the transitions J=2-1 and J=3-2 of CO, respectively. For both lines, the intensities are dependent mostly on the density, and show change with radiation field strength only at high n_H and high G_0.

The low J transitions in CO are very easily seen, due to the relatively low upper level energies and critical densities. Therefore, these transitions easily become optically thick, and we need to look at the mid-J and high-J transitions. In our observations, we have used the J=3-2 transition in CO. Ratios of intensities of higher-J transitions J=4-3 and J=6-5 to the intensity of CO J=3-2 are shown in figures 6.21 and 6.22, respectively. Both ratios show
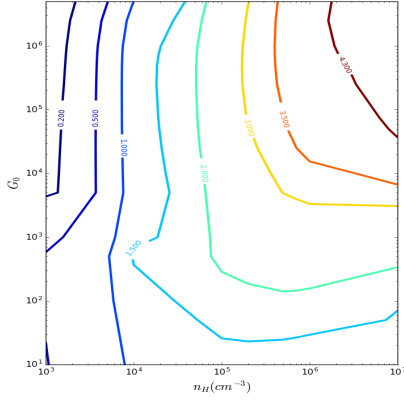
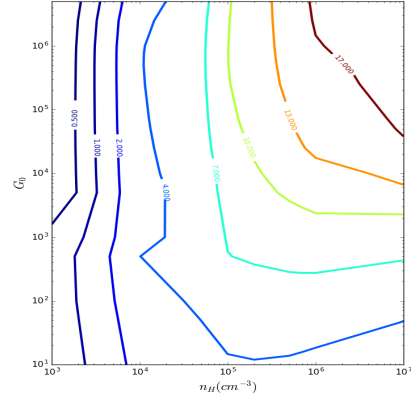Figure 6.19: Intensity of transition CO J=2-1, in 10^{-6}ergs cm^{-2}s^{-1}sr^{-1}

Figure 6.20: Intensity of transition CO J=3-2, in 10^{-6}ergs cm^{-2}s^{-1}sr^{-1}
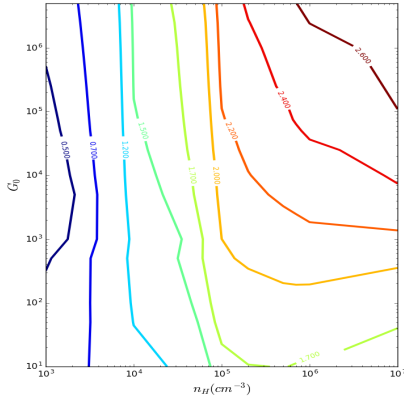

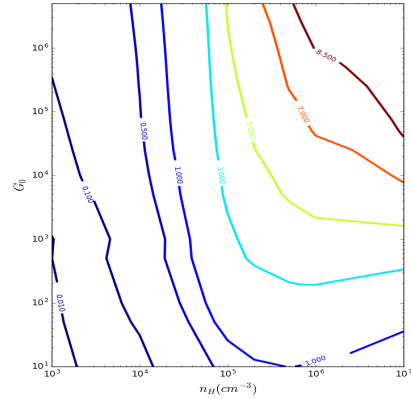Figure 6.21: Ratio of intensities of the transitions J=4-3 to J=3-2 for CO

Figure 6.22: Ratio of intensities of the transitions J=6-5 to J=3-2 for CO

strong dependence with density, specially for low n_H, and can be therefore used as a density indicator.

6.3 Effect of Metallicity

Across different galaxies, different metallicity environments have been observed. Pagel et al., 2003 [41] reports a spread in metallicities observed inside the Local Group. Even within the Milky Way, we can see a metallicity gradient (Sestito et al., 2007 [46] and 2008 [47],

Pace et al., 2008 [40], Villanova et. al, 2005 [51], Carraro et al., 2004 [4] and 2007 [5]). Since metal abundance in a galaxy depends on its rate of star formation, high-redshift galaxies and dwarf galaxies generally have a lower metallicity environment. (High-z (early universe) galaxies : Maiolino et al., 2008 [33], Oey and Kennicutt, 1993 [39], and Cresci et al., 2010 [8]. For dwarf galaxies, see Lequeux et al., 1979 [30], Searle and Sargent, 1972 [45], Rémy-Ruyer et al., 2013 [42]). The nearest dwarf galaxies, the Small and Large Magellanic Clouds(SMC LMC), show metallicities lower than 0.2-0.5 of solar standard (References for LMC metallicity : Choudhury et al., 2016 [6], Cole et al., 2005 [7] and Swaelmen et al., 2013 [50]; for SMC : Dias et al., 2010 [11] and Kayser et al., 2006 [25]). On the other hand, young star-burst galaxies show higher than solar metallicity (Wardlow et al., 2017 [52]). We see super-solar metallicities in case of AGNs(Active Galactic Nuclei), as well (Maiolino et al.,2006 [34]). Even towards the centre of the Milky Way, there is evidence of metallicities upto 3 times that of solar neighbourhood (Ryde et at al., 2016 [44], Rich et al., 2017 [43], Feldmeier-Krause et al., 2017 [14], Tuan Do et al., [12]).

Due to the wide range of metallicity values observed, it is interesting to study if the metallicity affects the distribution of the gas in a cloud.

In order to study the affect of metallicity of distribution of gas inside PDRs, we have run the Meudon PDR code for metallicity $Z = 0.5$ and $Z = 1.9$, and compare the results with that from $Z = 1$ metallicity models. In Figure 6.23(a), we show the comparison between intensities of [CII] 158 μm line and J=2-1 transition of CO. From figures and discussion in Section 6.2.3, we see that the mid-J transitions in CO have higher intensity and are less likely to be optically thick. Therefore, we also present comparison of [CII] 158 μm intensity to the intensities of J=3-2, J=4-3 and J=6-5 transitions of CO in Figure 6.23. Rarer isotopologues of CO are generally optically thin for larger range of parameter space. Hence, it might be useful to also look at the relative strengths of [CII] with transitions of these rarer isotopologues. In Figure 6.24 and Figure 6.25, we present comparisons of [CII] intensity with that of J=2-1 and J=3-2 transitions of ^{13}CO and C^{18}O, respectively.

From the figures, it can be seen that the effect of metallicity on the intensities of the CO transitions considered, is very small. On the other hand, lowering the metallicity from 1.9 to 1, and to 0.5 solar values, results in a substantial increase in the [CII] intensity, especially at higher densities and lower radiation field. The increase in [CII] intensity with decreasing metallicity, is most prominent for $n_H = 10^6$ cm^{-3} and 10^7 cm^{-3}, and $G_0 \leq 10^4$. At these conditions, a decrease in the metallicity by a factor of 2, results in an increase in the [CII] intensity by the same factor. At $G_0 = 10^6$, the [CII] intensity approaches saturation. At

lower metallicity, shielding is poor, and the ionising radiation has a better penetration to the cloud. Thus, CO is photo-dissociated deeper into the cloud, and the C^+ region extends further. As described in sections 6.2.2 and 6.2.3, intensity of [CII] 158 μm increases with G_0 and decreases with density. For low-J transitions of CO, the intensities remain roughly constant with varying G_0, and increases slowly with density. For higher-J transitions, the increase in intensity with density is more, and we also see an increase with G_0.

The difference in the transitions for the isotopologues of CO is observed best for low-J transitions. Assuming the transition from both ^{13}CO and $C^{18}O$ to be thin, it implies that the intensity calculated is seen from the entire column of gas in the cloud. For a given density, as G_0 is increased, more of the CO is dissociated, and there is a depletion in the CO column. This does not affect the intensity of the low-J transitions of CO, as they are optically thick; but for ^{13}CO and $C^{18}O$, this means a reduction of the effective column length emitting the radiation. Hence, a decrease of the J=2-1 and J=3-2 transitions can be seen for ^{13}CO and $C^{18}O$ in figures 6.24 and 6.25. This effect is most profound at low density and low metallicity, which lead to poor shielding, and hence better penetration of the FUV photons. Intensities of higher-J transitions increase slghtly with G_0, and so, this effect is slightly weaker in the J=3-2 transition.
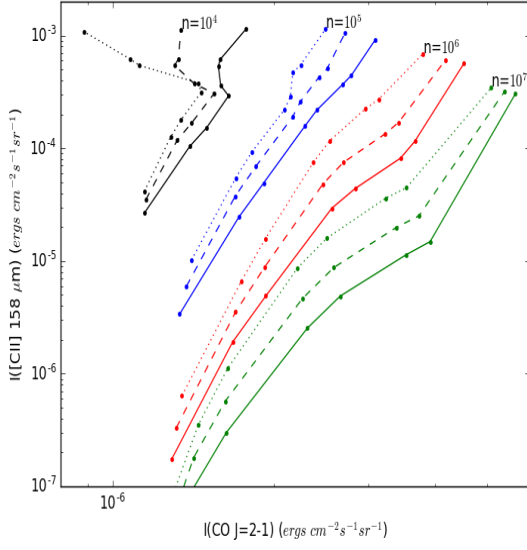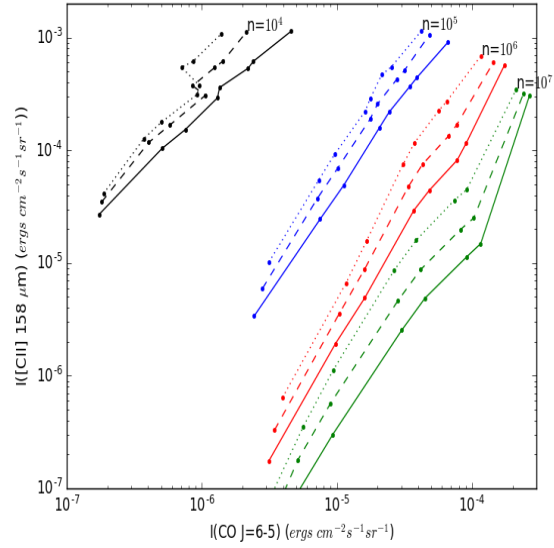
(a) $I_{[CII]158\ \mu m}$ vs $I_{CO\ J=2-1}$
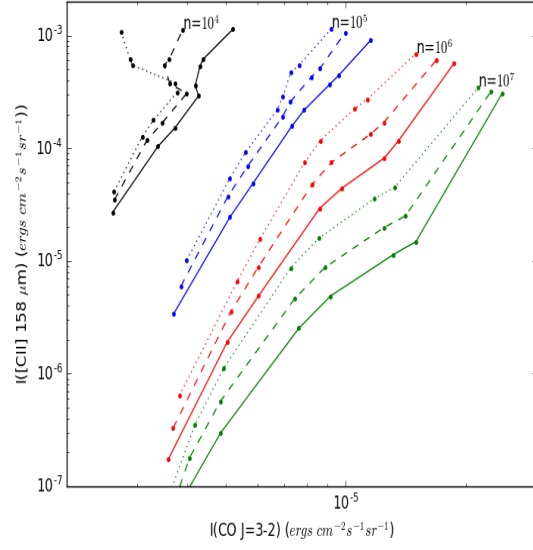
(b) $I_{[CII]158\ \mu m}$ vs $I_{CO\ J=3-2}$
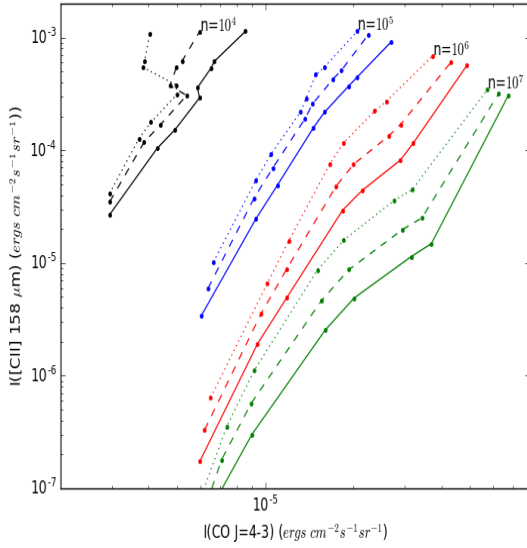
(c) $I_{[CII]158\ \mu m}$ vs $I_{CO\ J=4-3}$

(d) $I_{[CII]158\ \mu m}$ vs $I_{CO\ J=6-5}$

Figure 6.23: Variation of intensity of [CII] as a function of intensities of different transitions of CO. The figures show a range in G_0, for different densities, as shown in figure. For each curve, in all the plots, the topmost point correspond to $G_0 = 10^6$, and the value of G_0 decrease downward. The points show $G_0 = 10^4, 5 \times 10^3, 10^3, 500, 100, 50$ and 10, in that order from bottom to top. The Dotted, dashed and solid lines correspond to Z=0.5, 1 and 1.9, respectively. Intensities below $\sim 10^{-7} \mathrm{ergs\ cm^{-2}s^{-1}sr^{-1}}$ is not shown, as that is too faint to observe.

(a) $I_{[CII]158 \; \mu m}$
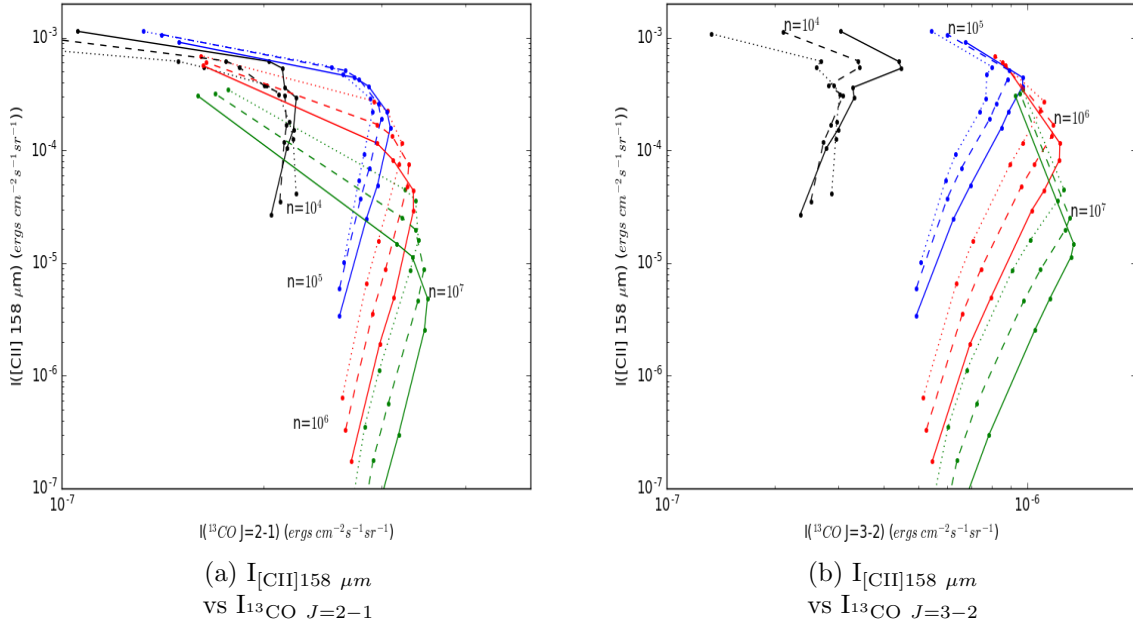vs $I_{^{13}CO \; J=2-1}$

(b) $I_{[CII]158 \; \mu m}$
vs $I_{^{13}CO \; J=3-2}$

Figure 6.24: Comparison of [CII] 158 μm to transitions J=1-0 and J=2-1 of ^{13}CO. The layouts are same as that in Figure 6.23
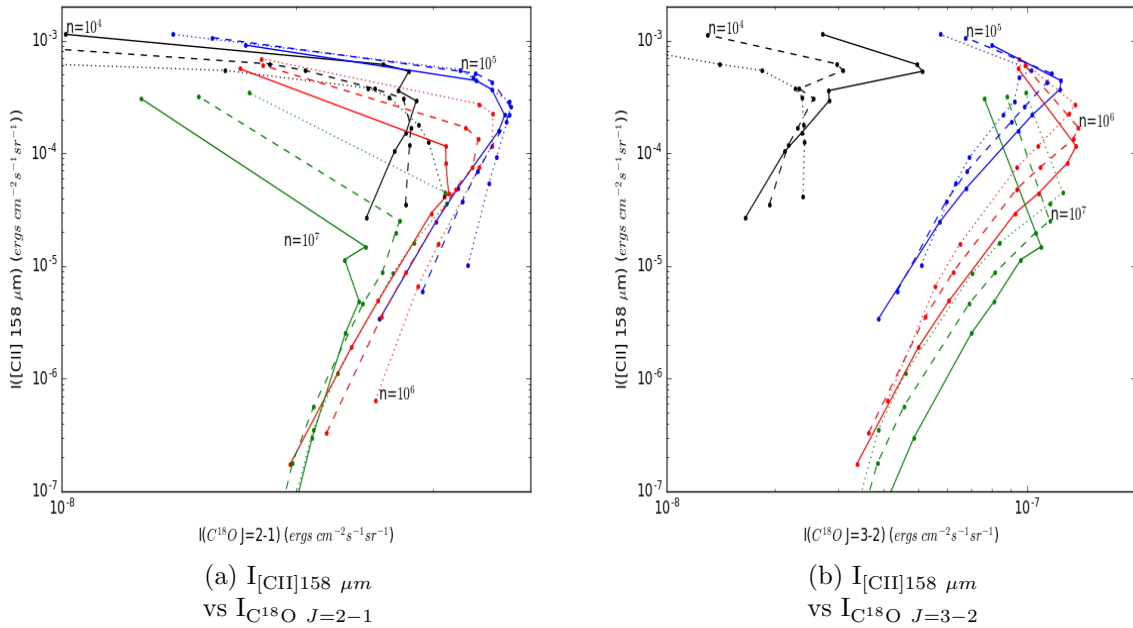

(a) $I_{[CII]158 \; \mu m}$
vs $I_{C^{18}O \; J=2-1}$

(b) $I_{[CII]158 \; \mu m}$
vs $I_{C^{18}O \; J=3-2}$

Figure 6.25: Comparison of [CII] 158 μm to transitions J=1-0 and J=2-1 of C^{18}O. The layouts are same as that in Figure 6.23

Chapter 7

Discussion and Summary

7.1 Physical conditions of the ρ Oph A PDR

In this section, we apply the results from the models using the Meudon PDR code, to guess on the physical conditions in the ρ Ophiuchus PDR, which we have studied in this project. As discussed in Chapter 3, we have looked at the [CII] 158 μm, [OI] 63 μm and 145 μm lines, and J=3-2 transitions in CO and its rarer isotopologues. To use these observations to predict possible density and radiation field in the PDR, we first select 17 positions, distributed fairly evenly throughout the [CII] region in ρ Oph PDR. These positions are shown in Figure 7.1, on a [CII] map. In order to have a good representative sample, we have selected positions around the [CII] peak, near the illuminating source S1, towards the outer envelope of the PDR, and near the molecular core. For each of these positions, we have computed ratios of intensities of CO J=3-2 and the [OI] transitions to [CII]. The range of these ratios are shown in Figure 7.2 and Figure 7.3. For [CII] and CO(and its isotopologues), the intensities shown here are the integrated intensities for velocity 0-7 km/s.

From Figure 7.2, the likely values for the PDR are $n_H \sim 10^5 - 10^6$, and $G_0 \sim 10^3 - 10^5$, from the overlap region of $I_{^{13}CO\ J=3-2}/I_{[CII]}$ and $I_{C^{18}O\ J=3-2}/I_{[CII]}$ ranges. Both ^{13}CO and C^{18}O are optically thin for most of the positions selected, unlike CO. This is possibly why the ratio with CO indicate a smaller density in the region, as the emission is not seen from the entire column.
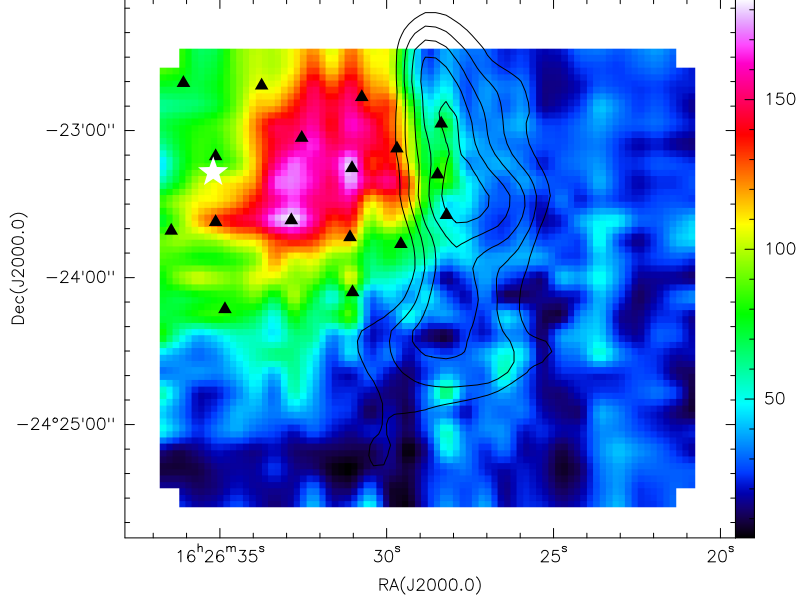
Figure 7.1: The 17 selected positions spread in the region, shown by black triangles. The colour map is for [CII] 158 μm, and the black contours show C^{18}O J=3-2 emission. The white star near the left edge show the position of the primary illuminating star, S1.

Figure 7.3 shows the range in ratio of [OI] transitions to [CII] in the region. The important difference between the two lines is that [OI] 63 μm is optically thick for the region, whereas the 145 μm line is optically thin for the most part. Therefore, we see no overlap between these two ratio ranges, and the ratio $I_{[OI]\ 63\ \mu m}/I_{[CII]\ 158\ \mu m}$ indicates a lower density.

7.2   Conclusion

The ρ Oph PDR is located in the molecular cloud L1688, which is the nearest region of star formation. The proximity of the region provides wonderful opportunity to study the region at high spatial resolution. In this project, we have studied the PDR located near the star S1, in velocity-resolved spectra of [CII], which primarily traces the hot, low density atomic region. We compare our observations with other dedicated PDR tracers, such as neutral oxygen and PAH molecules, and find that these species trace roughly the same region. The extent of the region agrees well with previous literature, as well. Comparison between tracers indicate in presence of inhomogeneous, clumpy distribution in the cloud. We also compare our observations with dense molecular gas tracer CO, which is seen to be emitted from the
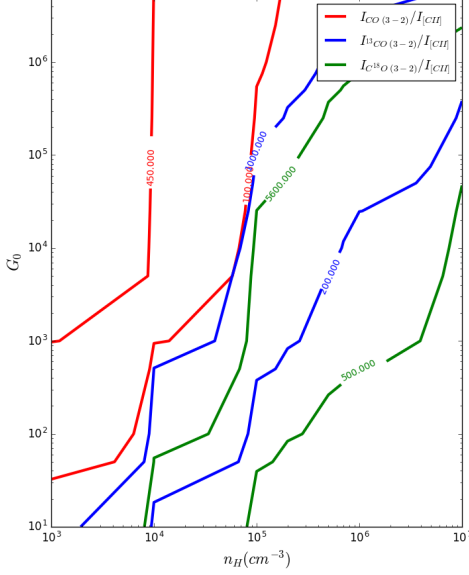
Figure 7.2: Ratios of intensities of CO and its isotopologues to the intensity of [CII] 158 μm. The contours of each colour show the range(for the ratio indicated in the plot), for the values at the 17 selected positions in ρ Oph PDR.
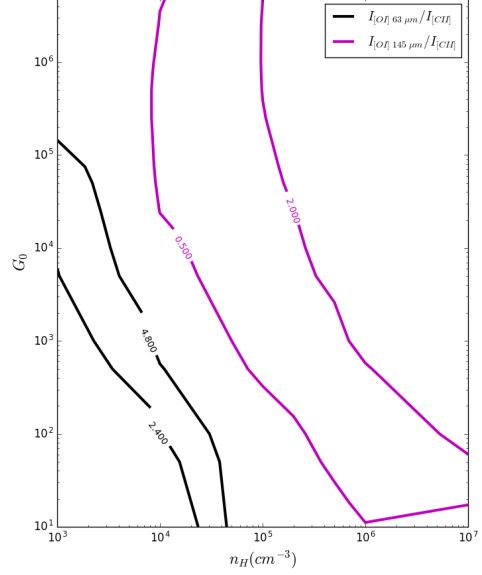

Figure 7.3: Ratios of intensities [OI] 63 μm and 145 μm, to the intensity of [CII] 158 μm. The contours of each colour show the range(for the ratio indicated in the plot), for the values at the 17 selected positions in ρ Oph PDR.

dense core lying outside the PDR.

We have used a numerical model, the Meudon PDR Code, to model clouds with a range of different physical properties, and use them to study variation of different observed intensities with density, incident FUV flux, and the metallicity. Using the results from the models, we are able to identify trends in line intensity and ratios. Calculation of line ratios correct for some of the observational bias, specially if the lines are emitted from the same region. Some of the line ratios are highly sensitive to either density or incident radiation strength, and therefore can be employed to determine the physical conditions in an observed region. We use our observed data to compare with the model generated results, and can predict that for the ρ Oph PDR, the most possible values of density and FUV radiation strength are $n_H \sim 10^5 - 10^6$ cm^{-3}, and $G_0 \sim 10^3 - 10^5$.

Bibliography

[1] J. H. Black. "Energy Budgets of Diffuse Clouds". In: *The First Symposium on the Infrared Cirrus and Diffuse Interstellar Clouds*. Ed. by R. M. Cutri and W. B. Latter. Vol. 58. Astronomical Society of the Pacific Conference Series. 1994, p. 355.

[2] E. Bron. "Stochastic processes in the interstellar medium". PhD thesis. LERMA, Observatoire de Paris, PSL Research University, CNRS, Sorbonne Universités, UPMC Univ. Paris 06, F-92190, Meudon, France ¡EMAIL¿emeric.bron@obspm.fr¡/EMAIL¿, 2014.

[3] J. R. Burke and D. J. Hollenbach. "The gas-grain interaction in the interstellar medium - Thermal accommodation and trapping". In: 265 (Feb. 1983), pp. 223–234. DOI: 10.1086/160667.

[4] G. Carraro et al. "Metal Abundances in Extremely Distant Galactic Old Open Clusters. I. Berkeley 29 and Saurer 1". In: 128 (Oct. 2004), pp. 1676–1683. DOI: 10.1086/423912. eprint: astro-ph/0406679.

[5] G. Carraro et al. "Old open clusters in the outer Galactic disk". In: 476 (Dec. 2007), pp. 217–227. DOI: 10.1051/0004-6361:20078113. arXiv: 0709.2126.

[6] S. Choudhury, A. Subramaniam, and A. A. Cole. "Photometric metallicity map of the Large Magellanic Cloud". In: 455 (Jan. 2016), pp. 1855–1880. DOI: 10.1093/mnras/stv2414. arXiv: 1510.05769.

[7] A. A. Cole et al. "Spectroscopy of Red Giants in the Large Magellanic Cloud Bar: Abundances, Kinematics, and the Age-Metallicity Relation". In: 129 (Mar. 2005), pp. 1465–1482. DOI: 10.1086/428007. eprint: astro-ph/0412389.

[8]   G. Cresci et al. "Gas accretion as the origin of chemical abundance gradients in distant galaxies". In: 467 (Oct. 2010), pp. 811–813. DOI: 10.1038/nature09451. arXiv: 1010.2534.

[9]   B. A. Croiset et al. "Mapping PAH sizes in NGC 7023 with SOFIA". In: 590, A26 (May 2016), A26. DOI: 10.1051/0004-6361/201527714. arXiv: 1603.02577.

[10]   I. Dabrowski. "The Lyman and Werner bands of H2". In: *Canadian Journal of Physics* 62 (Dec. 1984), pp. 1639–1664. DOI: 10.1139/p84-210.

[11]   B. Dias et al. "Age and metallicity of star clusters in the Small Magellanic Cloud from integrated spectroscopy". In: 520, A85 (Sept. 2010), A85. DOI: 10.1051/0004-6361/200912894. arXiv: 1002.4301 [astro-ph.SR].

[12]   T. Do et al. "Super-solar Metallicity Stars in the Galactic Center Nuclear Star Cluster: Unusual Sc, V, and Y Abundances". In: 855, L5 (Mar. 2018), p. L5. DOI: 10.3847/2041-8213/aaaec3. arXiv: 1802.08270.

[13]   S. R. Federman, A. E. Glassgold, and J. Kwan. "Atomic to molecular hydrogen transition in interstellar clouds". In: 227 (Jan. 1979), pp. 466–473. DOI: 10.1086/156753.

[14]   A. Feldmeier-Krause et al. "KMOS view of the Galactic Centre - II. Metallicity distribution of late-type stars". In: 464 (Jan. 2017), pp. 194–209. DOI: 10.1093/mnras/stw2339. arXiv: 1610.01623.

[15]   M. Gagné, S. L. Skinner, and K. J. Daniel. "Simultaneous Chandra and Very Large Array Observations of Young Stars and Protostars in ρ Ophiuchus Cloud Core A". In: 613 (Sept. 2004), pp. 393–415. DOI: 10.1086/422828. eprint: astro-ph/0405467.

[16]   J. R. Goicoechea and J. Le Bourlot. "The penetration of Far-UV radiation into molecular clouds". In: 467 (May 2007), pp. 1–14. DOI: 10.1051/0004-6361:20066119. eprint: astro-ph/0702033.

[17]   P. F. Goldsmith et al. "Herschel Measurements of Molecular Oxygen in Orion". In: 737, 96 (Aug. 2011), p. 96. DOI: 10.1088/0004-637X/737/2/96. arXiv: 1108.0441.

[18]   P. F. Goldsmith et al. "O_2 in Interstellar Molecular Clouds". In: 539 (Aug. 2000), pp. L123–L127. DOI: 10.1086/312854.

[19]   M. Gonzalez Garcia et al. "Radiative transfer revisited for emission lines in photon dominated regions". In: 485 (July 2008), pp. 127–136. DOI: 10.1051/0004-6361:200809440.

[20] L. G. Henyey and J. L. Greenstein. "Diffuse radiation in the Galaxy". In: 93 (Jan. 1941), pp. 70–83. DOI: 10.1086/144246.

[21] D. J. Hollenbach and A. G. G. M. Tielens. "Photodissociation regions in the interstellar medium of galaxies". In: *Rev. Mod. Phys.* 71 (1 Jan. 1999), pp. 173–230. DOI: 10.1103/RevModPhys.71.173. URL: https://link.aps.org/doi/10.1103/RevModPhys.71.173.

[22] K. E. Jameson et al. "First Results from the Herschel and ALMA Spectroscopic Surveys of the SMC: The Relationship between [C II]-bright Gas and CO-bright Gas at Low Metallicity". In: 853, 111 (Feb. 2018), p. 111. DOI: 10.3847/1538-4357/aaa4bb. arXiv: 1801.03518.

[23] J. J. Jensen et al. "PAH features within few hundred parsecs of active galactic nuclei". In: 470 (Sept. 2017), pp. 3071–3094. DOI: 10.1093/mnras/stx1447. arXiv: 1706.04811.

[24] M. J. Kaufman et al. "Far-Infrared and Submillimeter Emission from Galactic and Extragalactic Photodissociation Regions". In: 527 (Dec. 1999), pp. 795–813. DOI: 10.1086/308102. eprint: astro-ph/9907255.

[25] A. Kayser et al. "The Age-Metallicity Relation of the SMC". In: *ArXiv Astrophysics e-prints* (July 2006). eprint: astro-ph/0607047.

[26] A. Laor and B. T. Draine. "Spectroscopic constraints on the properties of dust in active galactic nuclei". In: 402 (Jan. 1993), pp. 441–468. DOI: 10.1086/172149.

[27] B. Larsson and R. Liseau. "Gas and dust in the star-forming region ρ Oph A. II. The gas in the PDR and in the dense cores". In: 608, A133 (Dec. 2017), A133. DOI: 10.1051/0004-6361/201731466. arXiv: 1709.00296.

[28] J. Le Bourlot et al. "Infrared and submillimetric emission lines from the envelopes of dark clouds". In: 267 (Jan. 1993), pp. 233–254.

[29] F. Le Petit et al. "A Model for Atomic and Molecular Interstellar Gas: The Meudon PDR Code". In: 164 (June 2006), pp. 506–529. DOI: 10.1086/503252. eprint: astro-ph/0602150.

[30] J. Lequeux et al. "Chemical composition and evolution of irregular and blue compact galaxies". In: 80 (Dec. 1979), pp. 155–166.

[31] R. Liseau et al. "Gas and dust in the star-forming region ρ Oph A. The dust opacity exponent β and the gas-to-dust mass ratio g2d". In: 578, A131 (June 2015), A131. DOI: 10.1051/0004-6361/201525641. arXiv: 1504.06277.

[32] R. Liseau et al. "Multi-line detection of O_2 toward ρ Ophiuchi A". In: 541, A73 (May 2012), A73. DOI: 10.1051/0004-6361/201118575. arXiv: 1202.5637.

[33] R. Maiolino et al. "AMAZE. I. The evolution of the mass-metallicity relation at z 3". In: 488 (Sept. 2008), pp. 463–479. DOI: 10.1051/0004-6361:200809678. arXiv: 0806.2410.

[34] R. Maiolino et al. "Metals and dust in high redshift AGNs". In: 77 (2006), p. 643. eprint: astro-ph/0603261.

[35] J. S. Mathis, P. G. Mezger, and N. Panagia. "Interstellar radiation field and dust temperatures in the diffuse interstellar matter and in giant molecular clouds". In: 128 (Nov. 1983), pp. 212–229.

[36] J. S. Mathis, W. Rumpl, and K. H. Nordsieck. "The size distribution of interstellar grains". In: 217 (Oct. 1977), pp. 425–433. DOI: 10.1086/155591.

[37] B. Mookerjea et al. "Study of photon dominated regions in Cepheus B". In: 456 (Sept. 2006), pp. 235–244. DOI: 10.1051/0004-6361:20064991. eprint: astro-ph/0606268.

[38] N. M. Murillo and S.-P. Lai. "Disentangling the Entangled: Observations and Analysis of the Triple Non-coeval Protostellar System VLA1623". In: 764, L15 (Feb. 2013), p. L15. DOI: 10.1088/2041-8205/764/1/L15. arXiv: 1301.5230.

[39] M. S. Oey and R. C. Kennicutt Jr. "Abundances of H II regions in early-type spiral galaxies". In: 411 (July 1993), pp. 137–152. DOI: 10.1086/172814.

[40] G. Pace, L. Pasquini, and P. François. "Abundances of four open clusters from solar stars". In: 489 (Oct. 2008), pp. 403–412. DOI: 10.1051/0004-6361:200809969. arXiv: 0806.2280.

[41] B. E. J. Pagel. "CNO Abundances in Dwarf and Spiral Galaxies (invited review)". In: *CNO in the Universe*. Ed. by C. Charbonnel, D. Schaerer, and G. Meynet. Vol. 304. Astronomical Society of the Pacific Conference Series. 2003, p. 187.

[42] A. Rémy-Ruyer et al. "Revealing the cold dust in low-metallicity environments. I. Photometry analysis of the Dwarf Galaxy Survey with Herschel". In: 557, A95 (Sept. 2013), A95. DOI: 10.1051/0004-6361/201321602. arXiv: 1309.1371 [astro-ph.CO].

[43] R. M. Rich et al. "Detailed Abundances for the Old Population near the Galactic Center. I. Metallicity Distribution of the Nuclear Star Cluster". In: *The Astronomical Journal* 154.6 (2017), p. 239. URL: http://stacks.iop.org/1538-3881/154/i=6/a=239.

[44] N. Ryde et al. "Chemical Evolution of the Inner 2 Degrees of the Milky Way Bulge: [fffdfffd/Fe] Trends and Metallicity Gradients". In: *The Astronomical Journal* 151.1 (2016), p. 1. URL: http://stacks.iop.org/1538-3881/151/i=1/a=1.

[45] L. Searle and W. L. W. Sargent. "Inferences from the Composition of Two Dwarf Blue Galaxies". In: 173 (Apr. 1972), p. 25. DOI: 10.1086/151398.

[46] P. Sestito, S. Randich, and A. Bragaglia. "Element abundances in the metal-rich open cluster NGC 6253". In: 465 (Apr. 2007), pp. 185–196. DOI: 10.1051/0004-6361:20066643. eprint: astro-ph/0701182.

[47] P. Sestito et al. "Open clusters as key tracers of Galactic chemical evolution. III. Element abundances in Berkeley 20, Berkeley 29, Collinder 261 and Melotte 66". In: 488 (Sept. 2008), pp. 943–958. DOI: 10.1051/0004-6361:200809650. arXiv: 0807.2313.

[48] M. Sizun et al. "Investigation of ZPE and temperature effects on the Eleyfffdfffdfff-dRideal recombination of hydrogen atoms on graphene using a multidimensional graphen-efffdfffdfffdHfffdfffdfffdH potential". In: *Chemical Physics Letters* 498.1 (2010), pp. 32–37. ISSN: 0009-2614. DOI: https://doi.org/10.1016/j.cplett.2010.08.039. URL: http://www.sciencedirect.com/science/article/pii/S0009261410011280.

[49] A. G. G. M. Tielens and D. Hollenbach. "Photodissociation regions. I - Basic model. II - A model for the Orion photodissociation region". In: 291 (Apr. 1985), pp. 722–754. DOI: 10.1086/163111.

[50] M. Van der Swaelmen et al. "Chemical abundances in LMC stellar populations. II. The bar sample". In: 560, A44 (Dec. 2013), A44. DOI: 10.1051/0004-6361/201321109. arXiv: 1306.4224.

[51] S. Villanova et al. "Metal Abundances in Extremely Distant Galactic Old Open Clusters. II. Berkeley 22 and Berkeley 66". In: 130 (Aug. 2005), pp. 652–658. DOI: 10.1086/430958. eprint: astro-ph/0504282.

[52] Julie L. Wardlow et al. "The Interstellar Medium in High-redshift Submillimeter Galaxies as Probed by Infrared Spectroscopy*". In: *The Astrophysical Journal* 837.1 (2017), p. 12. URL: http://stacks.iop.org/0004-637X/837/i=1/a=12.

[53] J. C. Weingartner and B. T. Draine. "Electron-Ion Recombination on Grains and Polycyclic Aromatic Hydrocarbons". In: 563 (Dec. 2001), pp. 842–852. DOI: 10.1086/324035. eprint: astro-ph/0105237.

[54] J. C. Weingartner and B. T. Draine. "Photoelectric Emission from Interstellar Dust: Grain Charging and Gas Heating". In: 134 (June 2001), pp. 263–281. DOI: 10.1086/320852. eprint: astro-ph/9907251.

[55] J. C. Weingartner, B. T. Draine, and D. K. Barr. "Photoelectric Emission from Dust Grains Exposed to Extreme Ultraviolet and X-Ray Radiation". In: 645 (July 2006), pp. 1188–1197. DOI: 10.1086/504420. eprint: astro-ph/0601296.

[56] Glenn J. White et al. "The James Clerk Maxwell telescope Legacy Survey of the Gould Belt: a molecular line study of the Ophiuchus molecular cloud". In: *Monthly Notices of the Royal Astronomical Society* 447.2 (2015), pp. 1996–2020. DOI: 10.1093/mnras/stu2323. eprint: /oup/backfile/content_public/journal/mnras/447/2/10.1093_mnras_stu2323/2/stu2323.pdf. URL: +%20http://dx.doi.org/10.1093/mnras/stu2323.

[57] M. G. Wolfire, D. Hollenbach, and C. F. McKee. "The Dark Molecular Gas". In: 716 (June 2010), pp. 1191–1207. DOI: 10.1088/0004-637X/716/2/1191. arXiv: 1004.5401.